OPAL Technical Note TN494
July 4, 1997

Limits on triple gauge boson couplings from the study of single W production in e^+e^- collisions at $\sqrt{s} = 161 - 172$ GeV

Christof Degenhart, Marco Verzocchi
University of Freiburg

Abstract

The measurement of the single W production through the reaction $e^+e^- \to We\overline{\nu}_e$ allows to measure the coupling between a photon and two W bosons. In this note we describe the selection of events of the $We\overline{\nu}_e$ type in e^+e^- collisions at $\sqrt{s} = 161 - 172$ GeV and derive a limit on the cross section, using only the hadronic decay channel of the W. From the cross section we derive limits on anomalous couplings at the γWW vertex.

1 Introduction

In 1996 LEP2 has reached center-of-mass energies of $\sqrt{s} = 161 - 172$ GeV allowing the production of W^+W^- boson pairs for the first time in e^+e^- collisions. The W^+W^- production cross section involves the triple gauge boson vertices between the W^+W^- and the Z^0 or photon. The measurement of these triple gauge boson couplings (TGCs) and the search for possible anomalous values is one of the principal physics goals at LEP2 [1]. To disentangle the relative contribution of the γWW and Z^0WW vertices and set limits on anomalous TGCs it is necessary to study the shape of the differential cross-section as a function of the $W^\pm$ production angle and of the helicity state of the W bosons. The $e^+e^- \rightarrow We\overline{\nu}_e$ production instead proceeds mainly through the fusion of a virtual W and a photon and is mostly sensitive to the value of the couplings at the γWW vertex [2, 3]. This process could in principle be observed also below the WW threshold, but the smallness of the cross-section and the limited luminosity available at 130-136 GeV do not allow to obtain stringent limits on the anomalous TGCs. Recently the L3 Collaboration has published a measurement of the cross section for single W production in e^+e^- collisions at $\sqrt{s} = 161 - 172$ GeV [4].

This note is organized as follows. We first describe Monte Carlo studies to analyse the sensitivity to anomalous TGCs in the $e^+e^- \rightarrow We\overline{\nu}_e$ channel using the data collected in 1996 with the OPAL detector at LEP2. We then describe the analysis procedure leading to the observation of four events with a signature compatible with that of single W production followed by its hadronic decay. Although the signature of the single W production followed by the leptonic decay of the W is peculiar (in most of the cases a single track in the detector), we prefer to concentrate on the hadronic decays of the W, given the smallness of the cross section and the limited luminosity. To extract limits on the cross section and on the anomalous couplings, a maximum likelihood fit to the observed number of events is then performed, taking into account the dependence of the $e^+e^- \rightarrow We\overline{\nu}_e$ cross section on the TGCs and also the presence of the background (but neglecting the dependence of the latter on the TGCs).

2 The single W production cross section

The $e^+e^- \rightarrow We\overline{\nu}_e$ reaction proceeds mainly through the fusion of a photon and a W boson emitted from the initial state electron and positron (diagram *a* in figure 1). In order to make up the W mass, one of the two bosons must have a large Q^2, and the lepton emitted at the same vertex is diffused at large angles. Since the intermediate state W cannot be too much off-shell, this happens mostly in the case of the neutrino. Thus a possible signature for single W events is that of an isolated lepton or a pair of jets originating from the decay of the W, accompanied by a large missing transverse momentum given by the neutrino and a final state electron scattered at small angles. This allows to enhance the contribution of the photon-W fusion tree level diagram with respect to the doubly resonant WW diagrams (the CC03 class, shown in figure 2), which at the energies of LEP2 give electrons contained mostly in the central part of the detector, and to reduce the sensitivity to the couplings at the Z^0WW vertex. In figure 3 we show the differential cross section at $\sqrt{s} = 172$ GeV for the $u\overline{d}e\overline{\nu}_e$ final state[1] with respect to the electron (or positron) direction and with respect to the invariant mass of the lepton pair, as well as the double differential cross section, both including all the diagrams contributing to the final state (empty histogram), or just the CC03 diagrams (hatched histogram), and requiring $M_{u\overline{d}} \approx M_W$. We observe that angular region where the single resonant contribution ($M_{e\nu_e} \neq M_W$) dominates is the forward scattering region ($\cos\theta_e \approx 1$).

Another reason to concentrate the study of the $e^+e^- \rightarrow We\overline{\nu}_e$ reaction to the kinematical region with electrons in the forward direction is connected to the reliability of the cross section prediction from Monte Carlo generators. In the Monte Carlo programs the value of α_{em} is kept fixed at some scale (usually definable from the user, although sometimes this involves also changing the value of $\sin^2\theta_w$). While for the CC03 diagrams the optimal scale for α_{em} is $Q^2 = 4{M_W}^2$, for the single

[1] Charge conjugation is implied throughout this note.

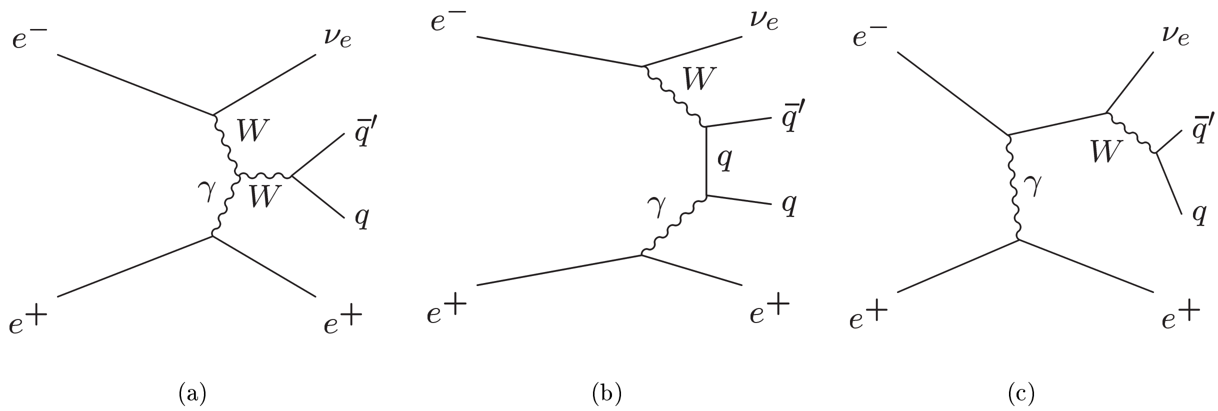

Figure 1: The diagrams dominating the $e^+e^- \to We\overline{\nu}_e$ final state.

resonant diagrams one should use two different values of α_{em} for the photon and for the W propagator [5]: the former should be evaluated at small Q^2. Since the Monte Carlo generators use only a single fixed value of α_{em}, an uncertainty of at least 5% is caused by the running of α_{em}, if the CC03 and the single resonant diagrams contribute equally to the cross section. This is not relevant for the data taken in 1996, but should be taken into account when the full LEP2 data set is analysed. This uncertainty can be strongly reduced if the contribution of the CC03 diagrams is suppressed relative to that of the single resonant diagrams.

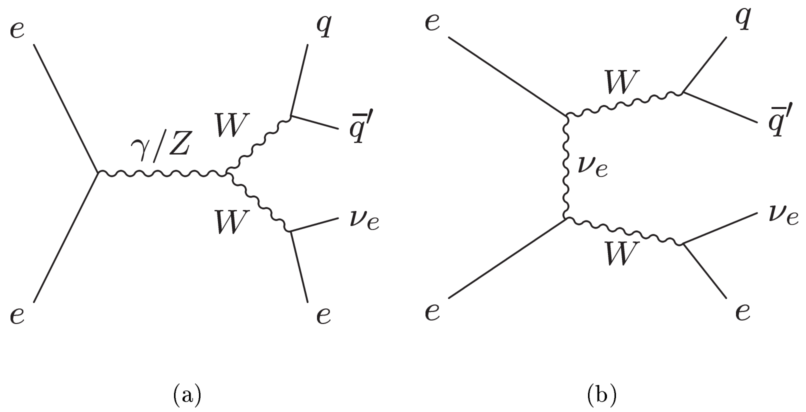

Figure 2: The CC03 diagrams.

We use the `grc4f` [6] Monte Carlo to study the dependency of the cross section for the $e^+e^- \to We\overline{\nu}_e$ final state with a topology compatible with that of single W production on the values of the γWW and Z^0WW couplings, by including all the 20 diagrams which lead to this final state[2]. We also use the same event generator to calculate the cross-sections obtained by taking single diagrams or summing only certain amplitudes. We can thus determine the order of magnitude of the relative contribution of the single diagrams to the total cross section and derive the kinematical cuts used to enhance the contribution of the $\gamma W^* \to W$ fusion process containing the γWW vertex, although this result may depend on the gauge used by the Monte Carlo generator.

We begin this Monte Carlo study by requiring that the final state electron is scattered at $|\cos\theta_e| \geq 0.98$, while the other charged fermions in the final state satisfy $|\cos\theta_f| < 0.98$. The cross section given

[2]The datacards used to run `grc4f` are given in appendix A.

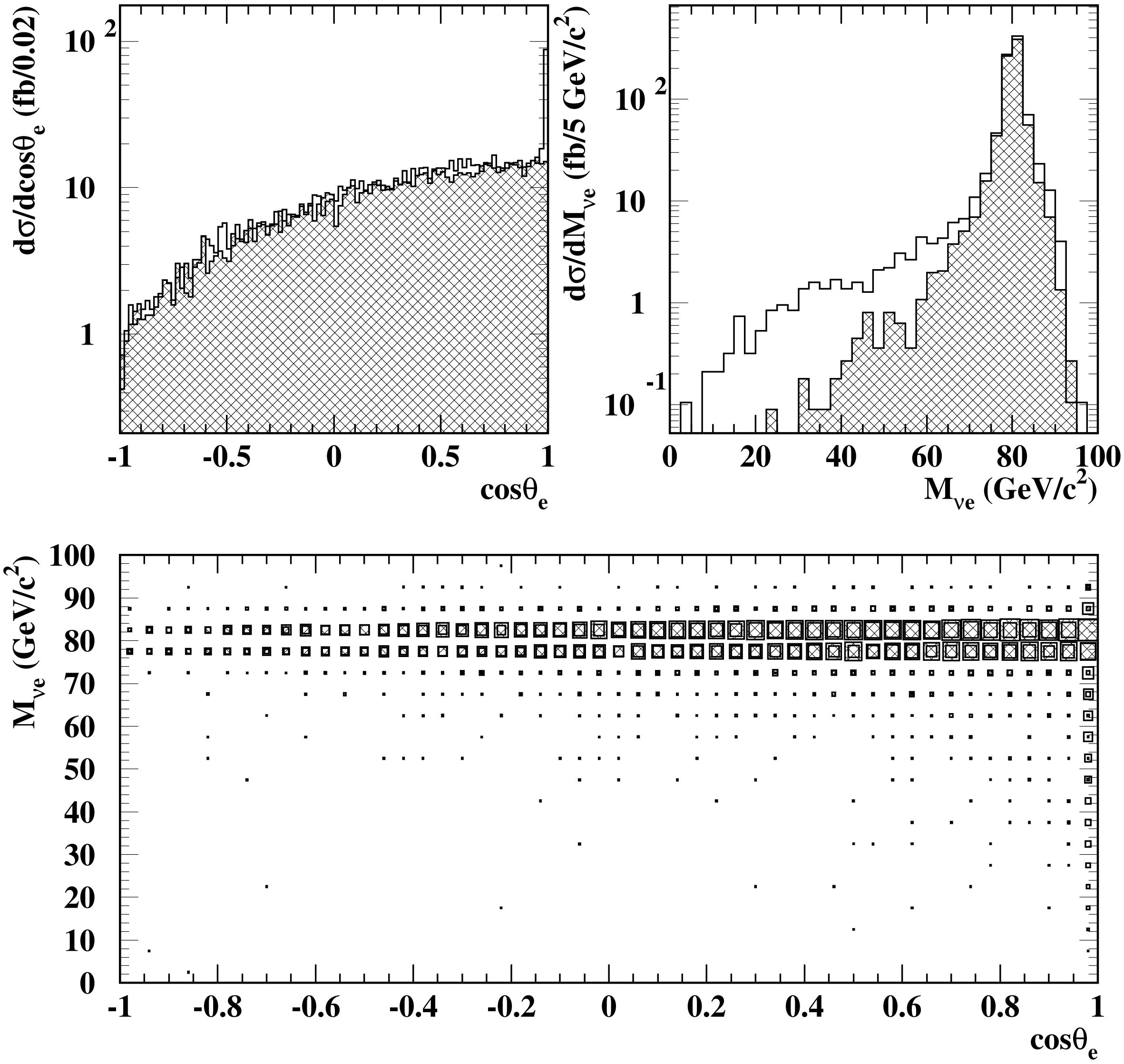

Figure 3: Differential cross section for the process $\mathrm{e^+e^-} \to \mathrm{u\bar{d}e\bar{\nu}_e}$ at $\sqrt{s} = 172$ GeV, with the requirement $M_{\mathrm{u\bar{d}}} \approx M_{\mathrm{W}}$. The empty histograms show the cross section calculated including all the diagrams, while the hatched histograms include only the CC03 diagrams. In the bottom plot the size of the boxes is proportional to the double differential cross section.

by grc4f for the $\mathrm{u\overline{d}e\overline{\nu}_e}$ final state under these kinematical constraint is given in table 1 for $\sqrt{s}$ =161 and 172 GeV. The cross section is dominated by the single W diagram, but relevant contributions are also given by the charged current deep inelastic scattering diagrams (non resonant $\mathrm{u\overline{d}}$ final state, diagram b in figure 1), and by the t-channel $\mathrm{e^+e^-} \to \mathrm{e^+e^-}$ diagram with final state radiation of a W boson (diagram c in figure 1). The contribution of the three diagrams where the intermediate photon is replaced by a $\mathrm{Z^0}$ is suppressed given the large value of $\mathrm{Z^0}$ mass, and the same happens for the diagram (similar to the one shown in figure 1c) where a W instead of a photon is exchanged in the t-channel. The CC03 diagrams give a minor contribution to the cross section, and among them the t-channel neutrino exchange dominates, giving thus a much reduced sensitivity to anomalous TGCs. The s-channel diagrams ($\mathrm{e^+e^-} \to \mathrm{f\overline{f}}$ followed by final state radiation of a W boson) are suppressed for a factor $\alpha_{\mathrm{em}}/(\sin\theta_w M_{\mathrm{W}})^2$ with respect to the $\mathrm{e^+e^-} \to \mathrm{f\overline{f}}$ process and are thus negligible.

Diagrams contributing	Cross section at 161 GeV (fb)	Cross section at 172 GeV (fb)
All diagrams	105.05 ±0.11	146.26 ±0.16
CC03 (Diagrams 2)	4.209±0.003	16.016±0.011
Diagrams 1a-c	101.89 ±0.11	130.97 ±0.12
Diagram 1a	177.83 ±0.12	230.32 ±0.14
Diagram 1b	21.326±0.022	23.464±0.024
Diagram 1c	56.340±0.056	69.618±0.061

Table 1: Cross section predictions from grc4f for the $\mathrm{u\overline{d}e\overline{\nu}_e}$ final state with the cuts $|\cos\theta_{\mathrm{e}}| > 0.98$ and $|\cos\theta_{(\mathrm{u,d})}| < 0.98$, summing the amplitude of all the diagrams, for the CC03 diagrams, for the diagrams in figure 1, first all together , and then separately.

The cross section obtained summing over all amplitudes is smaller than the sum of the contribution of all the diagrams: negative interference arises according to the number of γWW vertices in the various diagrams (in the Feynman rules this vertex has a minus sign relative to all the other fermion-fermion-boson and triple-boson vertices). Also the contribution to the cross section from the three diagrams shown in figure 1 shows a large negative interference, mainly between the single W diagram and the W FSR diagram. Even with kinematical cuts it is not possible to separate the contribution from these two diagrams. We show in figure 4 the differential cross section of $\mathrm{e^+e^-} \to \mathrm{u\overline{d}e\overline{\nu}_e}$ process, together with the separate contribution from single diagrams. The differential cross section for the single W diagram (1a) has almost the same shape of that of the W FSR diagram (1c), whereas the charged current deep inelastic scattering (1b) peaks at low invariant masses ($M_{\mathrm{u\overline{d}}} < 70$ GeV/c^2).

In the analysis procedure we require a veto on large energy deposits in the forward calorimeters, and this is equivalent to a cut on the angle of the scattered electron, implying that the selection efficiency drops to small values for angles above this cut. For this reason we prefer to adopt a tighter angular cut in the definition of the single W process. As a consequence, the contribution of the CC03 diagrams to the measured cross section is also reduced.

In the remainder of this note we use the following as definition of the single W process:

- $|\cos\theta_{\mathrm{e}}| > 0.995$,
- $|\cos\theta_{(\mathrm{q,\overline{q}'})}| < 0.98$,
- $70 < M_{\mathrm{q\overline{q}'}} < 90$ GeV/c^2.

In table 2 we show the cross section for the $\mathrm{u\overline{d}e\overline{\nu}_e}$ final state for $\sqrt{s}$ =161 and 172 GeV, for this new definition of the single W signal. With respect to the previous definition shown in table 1 the cross section is reduced by approximately 30%, but the contribution of the CC03 diagrams and of the non resonating diagram are largely reduced.

The contribution of the CC03 diagrams could be reduced even further by making an harder cut on the direction of the forward scattered electron. However this will introduce an additional uncertainty,

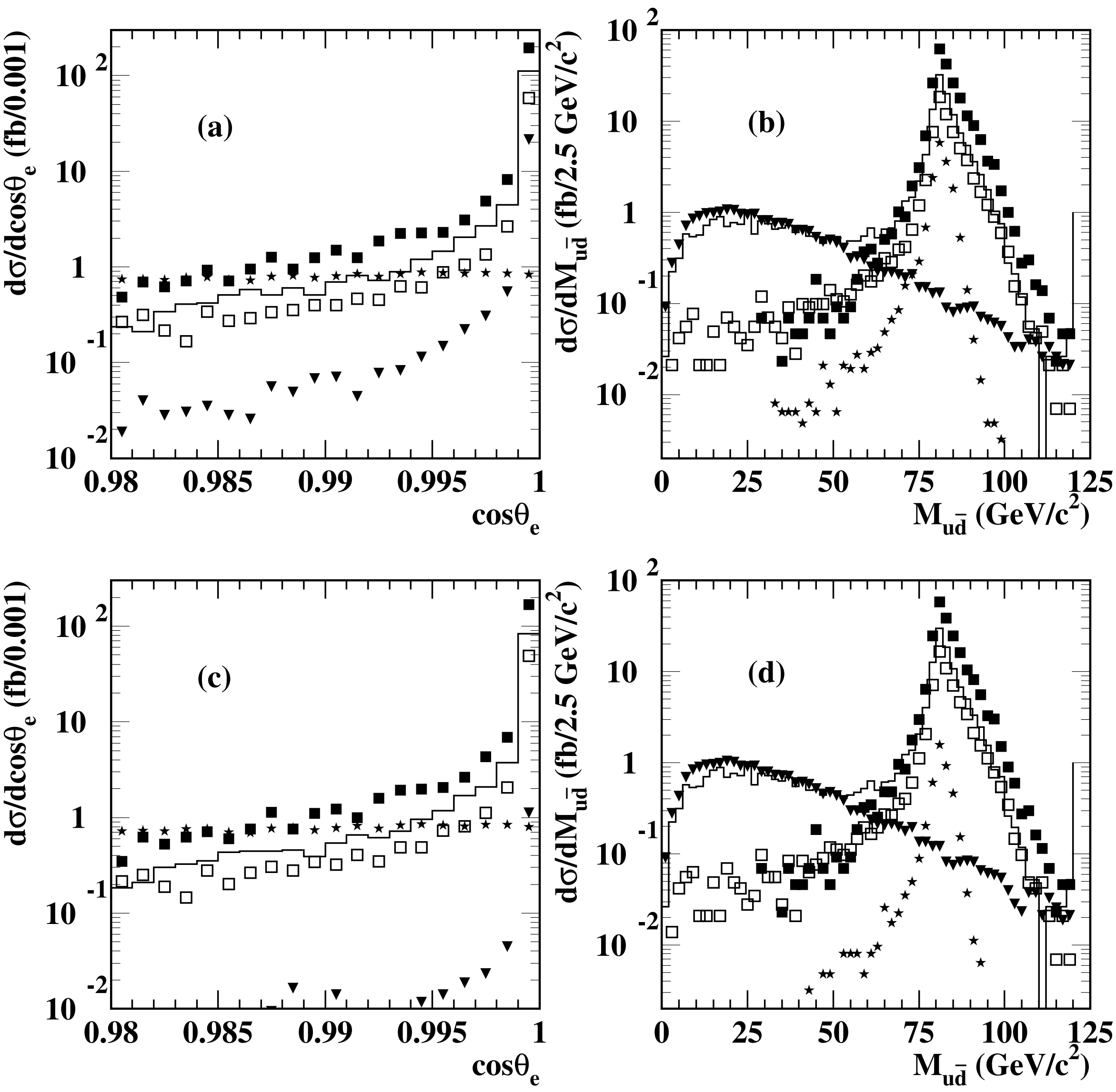

Figure 4: Differential cross section for the process $e^+e^- \to u\bar{d}e\bar{\nu}_e$at $\sqrt{s} = 172$ GeV.The empty histogram show the cross sections calculated including all the diagrams, the full boxes (■) including only the single W diagram, the empty boxes (□) including only the W FSR diagram, the stars ($\star$) including only the CC03 diagrams and the full triangles (▼) including only the non resonant diagram. In a) and b) the differential cross sections are shown before any other cut is applied, whereas in c) we require $M_{u\bar{d}} < 70$ GeV$/c^2$ and in d) we require $|\cos\theta_e| \geq 0.995$.

since the transverse momentum of the electron depends on the correct description of the initial state radiation. Differences of the order of 10% between the two methods[3] available in `grc4f` for the description of the initial state radiation appear in the cross section if the angular cut is placed above $|\cos\theta_e| \approx 0.998$.

Diagrams contributing	Cross section at 161 GeV (fb)	Cross section at 172 GeV (fb)
All diagrams	73.2 ±0.6	97.4 ±0.8
CC03 (Diagrams 2)	1.00±0.02	4.12±0.01
Diagrams 1a-c	71.5 ±0.6	92.1 ±0.7
Diagram 1a	145.7 ±0.8	184.4 ±1.0
Diagram 1b	1.04±0.05	1.21±0.05
Diagram 1c	44.7 ±0.3	54.0 ±0.3

Table 2: Cross section predictions from `grc4f` for the $\mathrm{u\overline{d}e\overline{\nu}_e}$ final state with the cuts $|\cos\theta_e| > 0.995$, $|\cos\theta_{(u,d)}| < 0.98$ and $70 < M_{u\overline{d}} < 90$ GeV$/c^2$, summing the amplitude of all the diagrams, for the CC03 diagrams, for the diagrams in figure 1, first all together, and then separately.

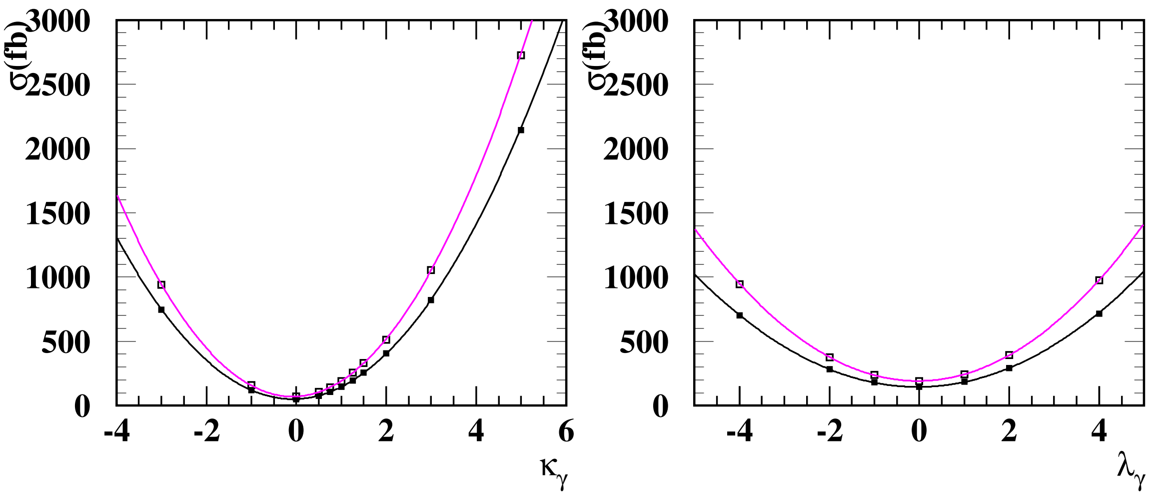

Figure 5: Cross section for the process $e^+e^- \to q\overline{q}'e\overline{\nu}_e$ as a function of the anomalous couplings κ_γ and λ_γ in the α model for $\sqrt{s} = 161$ GeV (lower curves - black lines), and for $\sqrt{s} = 172$ GeV (upper curves - gray lines), the other parameter being fixed at its Standard Model value. The points represent the values computed with the `grc4f` Monte Carlo generator, while the line indicate a quadratic interpolation between these values. The Standard Model cross section is obtained for $\kappa_\gamma = 1$ and $\lambda_\gamma = 0$.

The dependence of the $e^+e^- \to q\overline{q}'e\overline{\nu}_e$ cross section for the kinematical cuts given above from the κ_γ and λ_γ couplings is shown[4] in figure 5 for $\sqrt{s}$ =161 and 172 GeV. The predicted cross section is always larger than in the Standard Model as long as only λ_γ is varied, while for certain values of κ_γ it can also be smaller then in the Standard Model. Given that the contribution of the diagrams involving the Z^0WW vertex is negligible, the cross section depends weakly on the other anomalous couplings

[3]In one approach a structure function formalism is applied (SF) and in the second approach a QED parton shower formalism is applied (PS). In the second case the ISR photons have a transverse momentum different from zero.

[4]The value of the cross section are tabulated in Appendix B.

(g_1^z, $\kappa_z$and λ_z), as shown in [3]. In computing with `grc4f` the cross section for the $e^+e^- \to We\overline{\nu}_e$ process we have assumed the constraints among the TGC proposed in [7], with $\alpha_{W\phi} = 0$. In this case $\lambda_\gamma = \lambda_z = \alpha_W$, $\kappa_\gamma = 1 + \alpha_{B\phi}$ and $\kappa_z = 1 + \alpha_{B\phi}\tan^2\theta_w$. We have also computed the cross section assuming a different relation among the anomalous couplings, commonly used by the $p\overline{p}$ experiments [8] $\lambda_\gamma = \lambda_z$ and $\kappa_\gamma = \kappa_z$, and varying only κ_γ leaving all other parameters fixed at the Standard Model values. The cross section for the $u\overline{d}e\overline{\nu}_e$ final state (using the first definition of the single W process) at $\sqrt{s} = 172$ GeV is shown in figure 6 as a function of κ_γ for the three models: only for large values of the anomalous couplings (already excluded by the present measurements [9]) is the difference between the models larger than 3%. Since this value is smaller than the precision we can aim at with the currently available data set, the limits on the anomalous couplings which we will derive in the following will be independent from the relation assumed between the γWW and the Z^0WW couplings.

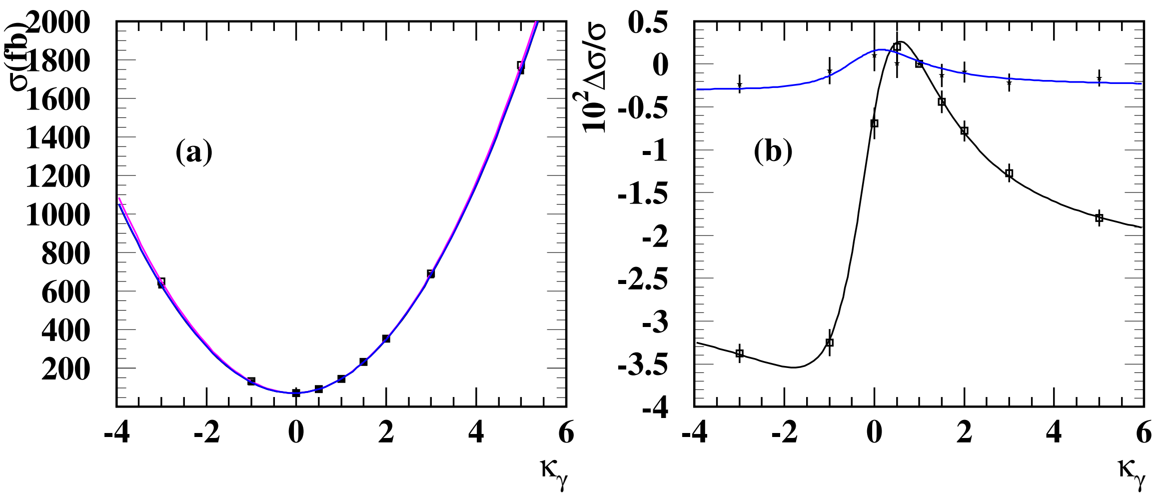

Figure 6: Cross section for the process $e^+e^- \to u\overline{d}e\overline{\nu}_e$ at $\sqrt{s} = 172$ GeV as a function of κ_γ in the α model (■), in the $\kappa_z = \kappa_\gamma$ model (□), and for a variation of κ_γ only, with all the other parameters fixed at the Standard Model value ($\star$) (a). The points represent the values computed using `grc4f` and the lines indicate a quadratic interpolation between these values. In (b) we show the relative difference in the cross section for the second two models (in%) relative to the α model.

To gain confidence in the `grc4f` predictions, we have calculated the cross section using also ERATO [10] and EXCALIBUR [11]. Contrary to `grc4f`, both these programs use massless matrix elements and some approximations [12] to avoid divergences in the integration of the differential cross section for small scattering angles of the outgoing electron. The default values of the physical parameters in these Monte Carlos are optimised for the calculation of the CC03 diagrams. As explained above a different value of α_{em} should be used when calculating the cross section in the kinematical region where the cross section is dominated by the single W diagram(s). In the improved Born approximation scheme used in `grc4f` this is simply accomplished by changing the value of α_{em}, whereas in EXCALIBUR and ERATO one has to change also the value of $\sin^2\theta_w$ according to the formula $\sin^2\theta_w = 4\pi\alpha_{em}/\sqrt{2}G_\mu M^2_{Z^0}$, keeping the value of G_μ fixed. The cross section calculated by the three programs are shown in table 3 and are in a reasonable agreement, the largest difference among them being of 10%. The `grc4f` matrix element has recently been introduced inside the KORALW Monte Carlo [13] and it would be interesting to compare the results of the two programs, given the different treatment of the initial state radiation. The comparison between different programs should also be extended to differential cross sections.

Monte Carlo	Cross section at 161 GeV (fb)	Cross section at 172 GeV (fb)
`grc4f` (SF)	73.2 ± 0.6	97.4 ± 0.8
`grc4f` (PS)	71.2 ± 0.7	94.7 ± 0.9
ERATO	75.9 ± 0.3	103.6 ± 0.6
EXCALIBUR	70.3 ± 0.9	94.6 ± 1.1

Table 3: Cross section predictions from different Monte Carlo generators for the $\mathrm{u\overline{d}e\overline{\nu}_e}$ final state with the cuts $|\cos\theta_{\mathrm{e}}| > 0.995$, $|\cos\theta_{(\mathrm{u,d})}| < 0.98$ and $70 < M_{\mathrm{u\overline{d}}} < 90$ GeV$/c^2$.

In summary, the expected cross section for $\mathrm{e^+e^- \to q\overline{q}'e\overline{\nu}_e}$ with the kinematical cuts made to enhance the contribution from the single W diagram(s) is approximately 145 fb at $\sqrt{s} = 161$ GeV and 190 fb at $\sqrt{s} = 172$ GeV (this values are obtained summing the cross section for the processes $\mathrm{e^+e^- \to u\overline{d}e\overline{\nu}_e}$ and $\mathrm{e^+e^- \to c\overline{s}e\overline{\nu}_e}$, neglecting the quark mixing). The expected number of events in the approximately 20 pb^{-1} data collected during 1996 is 3.5. At $\sqrt{s} = 161(172)$ GeV the single W cross section is a factor of 25(60) smaller than the W pair cross section, and 1000(650) smaller than the $\mathrm{e^+e^- \to q\overline{q}}$ cross section. Given the limited luminosity available it is not expected that a cross section measurement could be performed. However an upper limit on the cross section could be set and translated into limits on the anomalous couplings κ_γ and λ_γ.

3 Data and Monte Carlo samples

For this note we have analysed a sample of 9.89 ± 0.06 pb^{-1} and a sample of 10.36 ± 0.06 pb^{-1} taken at the luminosity weighted center-of-mass energies of $\sqrt{s} = 161.30 \pm 0.06$ and $\sqrt{s} = 172.12 \pm 0.06$ GeV/c^2 [14] respectively, collected in 1996. To simulate the signal we use the `grc4f` Monte Carlo, with the hadronisation performed using JETSET [15] and using both available methods for generating initial state radiation.

We use as a reference sample to simulate the $\mathrm{e^+e^- \to q\overline{q}}$ background the PYTHIA [15] Monte Carlo, and cross check its predictions using HERWIG [16]. The Monte Carlo cross section for these samples is scaled to the ZFITTER [17] prediction. Hadronic events produced in low Q^2 (untagged) $\gamma\gamma$ collisions are simulated using PHOJET [18], and cross checked with PYTHIA, whereas for high Q^2 (tagged) $\gamma\gamma$ hadronic events we use HERWIG as reference sample and PYTHIA or TWOGEN [19] for cross checks. Four fermion backgrounds are simulated using either `grc4f` as main sample (with EXCALIBUR used for cross checks), skipping in both cases the $\mathrm{e^+e^-q\overline{q}}$ final state. Both this samples are generated at $\sqrt{s} = 171$ instead of 172 GeV. Since out main background is represented by $\mathrm{W^+W^- \to q\overline{q}'\ell\overline{\nu}_\ell}$ decays, we scale the cross section of these samples by the ratio of the $\mathrm{e^+e^- \to W^+W^-}$ cross sections at the two center-of-mass energies. To avoid double counting, the $\mathrm{e^+e^-q\overline{q}}$ final state is simulated adding to the $\gamma\gamma$ Monte Carlo samples, the $\mathrm{e^+e^- \to Z^0e^+e^-}$ sample generated with `grc4f` and the s-channel $\mathrm{e^+e^-q\overline{q}}$ sample generated with FERMISV [20]. As a cross check we use the same samples, including other Monte Carlo runs generated with `grc4f` or EXCALIBUR and perform a separation based on angular cuts for the final state electrons, as explained in [21]. To avoid double counting between the signal and background in the $\mathrm{q\overline{q}'e\overline{\nu}_e}$ final state, we skip in the background Monte Carlo sample the events which have a kinematical configuration which would be accepted as signal using the first definition of single W events introduced in section 2, and then split the sample generated with `grc4f` into signal and background using the second definition of single W events (with tighter angular cuts and with the invariant mass cut). Since our selection is biased towards high multiplicities and high invariant masses we neglect the background coming from lepton pairs produced through $\mathrm{Z^0}/\gamma$ annihilation or $\gamma\gamma$ reactions. The list of the Monte Carlo samples used for the background are given in Appendix C.

4 Event selection

We start our analysis by performing a general selection of multihadronic events. We require that the event contains at least 6 good quality tracks and 8 good quality clusters in the electromagnetic calorimeter. This cut removes almost completely the events with four leptons in the final state. To reject beam gas interactions we require that the fraction of good quality tracks and clusters in the electromagnetic calorimeter are both larger than 20%. As quality criteria we adopt those used for the selecton of $W^+W^- \rightarrow q\overline{q}'\ell\overline{\nu}_\ell$ events as implemented in the WW110 processor [22]. In each event two jets are reconstructed using all tracks and calorimeter clusters (both electromagnetic and hadronic), using the Durham [23] recombination scheme. Only events which satisfy the cut $y_{23} < 0.03$ are further analysed, y_{23} being the value of the jet resolution parameter at which an event is reclassified from 3 to 2 jets. This cut removes almost all $W^+W^- \rightarrow q\overline{q}'q\overline{q}'$ decays and a large fraction of the $W^+W^- \rightarrow q\overline{q}'\ell\overline{\nu}_\ell$ events, given that the lepton in these events will be usually reconstructed as a third well separated jet. We also require that each jet is constituted by at least two good charged tracks and two unassociated clusters in the electromagnetic calorimeter. We reconstruct the energy and the direction of the jets using the GCE++ algorithm [24] to avoid double counting. Finally we require the invariant mass of the two jet system to be larger than 12 GeV/c^2, to reduce the amount of hadronic events originated in $\gamma\gamma$ collisions. This preselection is 80% efficient for the $e^+e^- \rightarrow q\overline{q}'e\overline{\nu}_e$ events satisfying the single W kinematical cuts, and results in samples of 2440 and 2661 events at $\sqrt{s} = 161$ and 172 GeV respectively. At this stage the background is constituted mostly from hadronic events originated from $\gamma\gamma$ collisions and $e^+e^- \rightarrow q\overline{q}$. The invariant mass of the two jet system is shown at this level of the analysis in figure 7 for the 1996 LEP2 data set, together with the Monte Carlo prediction of the background and of the expected signal assuming that the couplings at the γWW vertex have the Standard Model values.

To further reject the hadronic events originated from $\gamma\gamma$ collisions, and to ensure that the jets are well contained, so that their energy and the missing momentum vector are correctely measured, we apply a veto on large energy deposits in the forward detectors, and require that at least one jet is found at large angle with respect to the beam direction. We also require that the particle which decays into the two jet system does not point in the beam direction. This cut helps reducing the radiative returns to the Z^0 peak, which give an invariant mass distribution peaking slightly above that of the signal, thus representing a dangerous background, given the poor mass resolution. The distribution of the energy deposited in the forward detector and in the silicon tungsten calorimeter is shown in figure 7, while the angular distribution of jets is shown in figure 8. We require (cut A):

- $E_{GC} \leq 10.0$ GeV (energy deposited in the gamma catchers),
- $E_{FD} \leq 10.0$ GeV (energy deposited in the forward calorimeters),
- $E_{SW} \leq 40.0$ GeV (energy deposited in the silicon tungsten calorimeters),

and (cut B):

- $\min(|\cos\theta_{j_1}|, |\cos\theta_{j_2}|) \leq 0.9$, being $\cos\theta_{j_i}$ the polar angle of the i^{th} jet,
- $|\cos\theta_{j_1}| + |\cos\theta_{j_2}| \leq 1.8$ and
- $|\cos\theta_{jj}| \leq 0.92$, being $|\cos\theta_{jj}|$ the reconstructed direction of the two jet system.

After these cuts 379 events at $\sqrt{s} = 161$ GeV and 329 events at $\sqrt{s} = 172$ GeV remain in the data, while 341 and 308 are predicted from the Monte Carlo. The background is at this stage dominated by the non radiative $e^+e^- \rightarrow q\overline{q}$ events. The efficiency for the signal is predicted to be approximately 63%. To isolate the events which have a kinematics similar to that of the single W

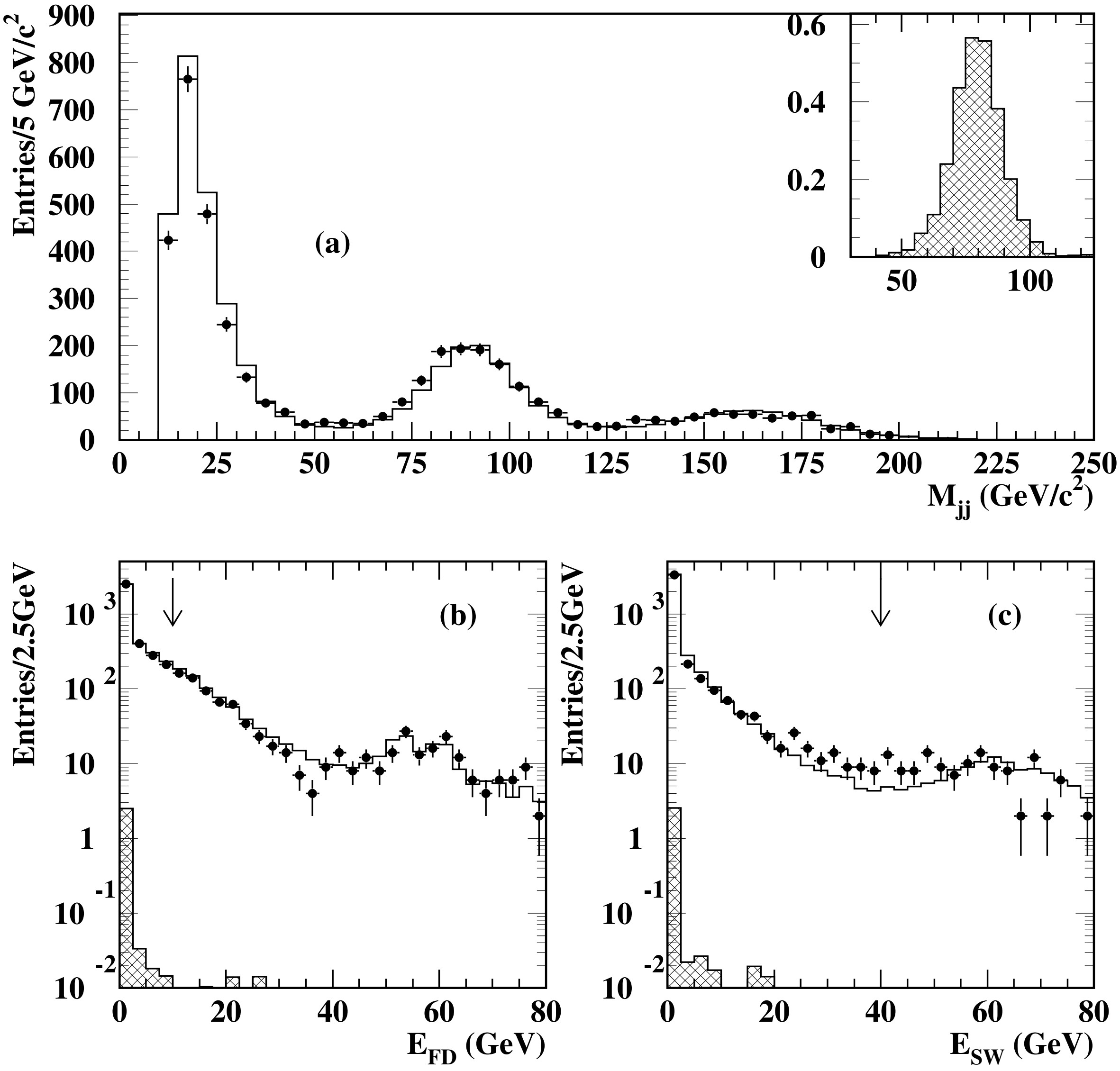

Figure 7: Invariant mass distribution (a) of the two jet system after the preselection for the 1996 data set (full points) and Monte Carlo background (histogram). The small inset shows the expectation (shaded histogram) of the single W signal. In b) and c) we show the distribution of the energy deposited in the forward detector and in the silicon tungsten calorimeter. The arrows indicate the position of the cuts.

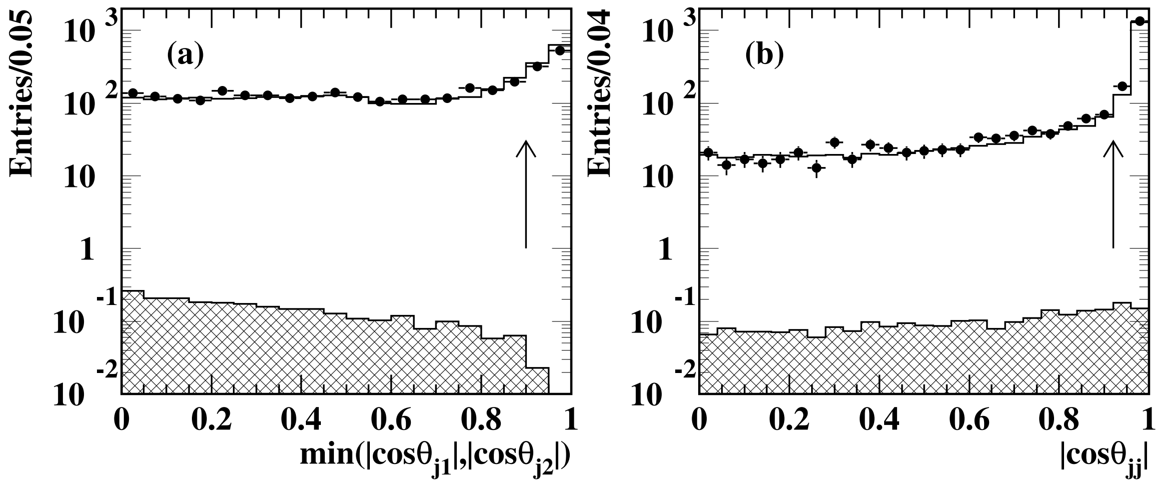

Figure 8: Angular distribution of jet being further from the beam axis (a), and of the reconstructed direction of the two jet system (b), after the cuts on the energy deposited in the forward detectors. The empty histogram represent the distribution of the background, the shaded one the expected distribution of the single W events and the full dots represent the events observed in the 1996 LEP2 data set. The arrows indicate the position of the cuts.

events we apply a cut on the missing transverse momentum and on the acoplanarity angle [5]. This cut reduces strongly the hadronic background arising from the $e^+e^- \to q\overline{q}$ reaction and from $\gamma\gamma$ collisions. The remaining background is then constituted from $W^+W^- \to q\overline{q}'\ell\overline{\nu}_\ell$ decays where the lepton is either lost or mismeasured. Above the threshold for W^+W^- production the W bosons will have a non negligible momentum and the two jets coming from the hadronic decay of one of the Ws will not appear as back to back. For this reason and since the cross section for the production of W^+W^- pairs is a factor of 4 larger at $\sqrt{s} = 172$ GeV than at $\sqrt{s} = 161$ GeV, the cut on the missing transverse momentum and on the acoplanarity is harder at higher energy. The missing transverse momentum is reconstructed using in the GCE++ algorithm all the detectors, including the forward calorimeters, whereas the acoplanarity is calculated using the jet directions previously defined. We perform a correlated cut on the two variables and lower the threshold on one of the variables, in case that the other one assumes large values. We require (cut C):

- $\not{p}_t \geq 10.0$ GeV/c, where $\not{p}_t$ is the missing transverse momentum,
- $\phi_{\mathrm{acop}} \geq 10^\circ$, where ϕ_{acop} is the acoplanarity angle, and
- $(\not{p}_t/1\ GeV/c)\ + 1.5(\phi_{\mathrm{acop}}/1^\circ) \geq 50$ if $\sqrt{s} = 161$ GeV, or
- $(\not{p}_t/1\ GeV/c)\ + 2.0(\phi_{\mathrm{acop}}/1^\circ) \geq 50$ if $\sqrt{s} = 172$ GeV.

The effect of this cut is shown is figure 9 for the ratio of the signal and background Monte Carlos at $\sqrt{s} = 161$ and 172 GeV. After this cut 3.6 events (of which 0.7 are signal) and 11.8 events (of which 1.1 are signal) are expected in the data at $\sqrt{s} = 161$ GeV and 172 GeV respectively, while 6 and 10

[5]The acoplanarity is defined as the complement to 180° of the angle between the two jets in the plane transverse to the beam axis.

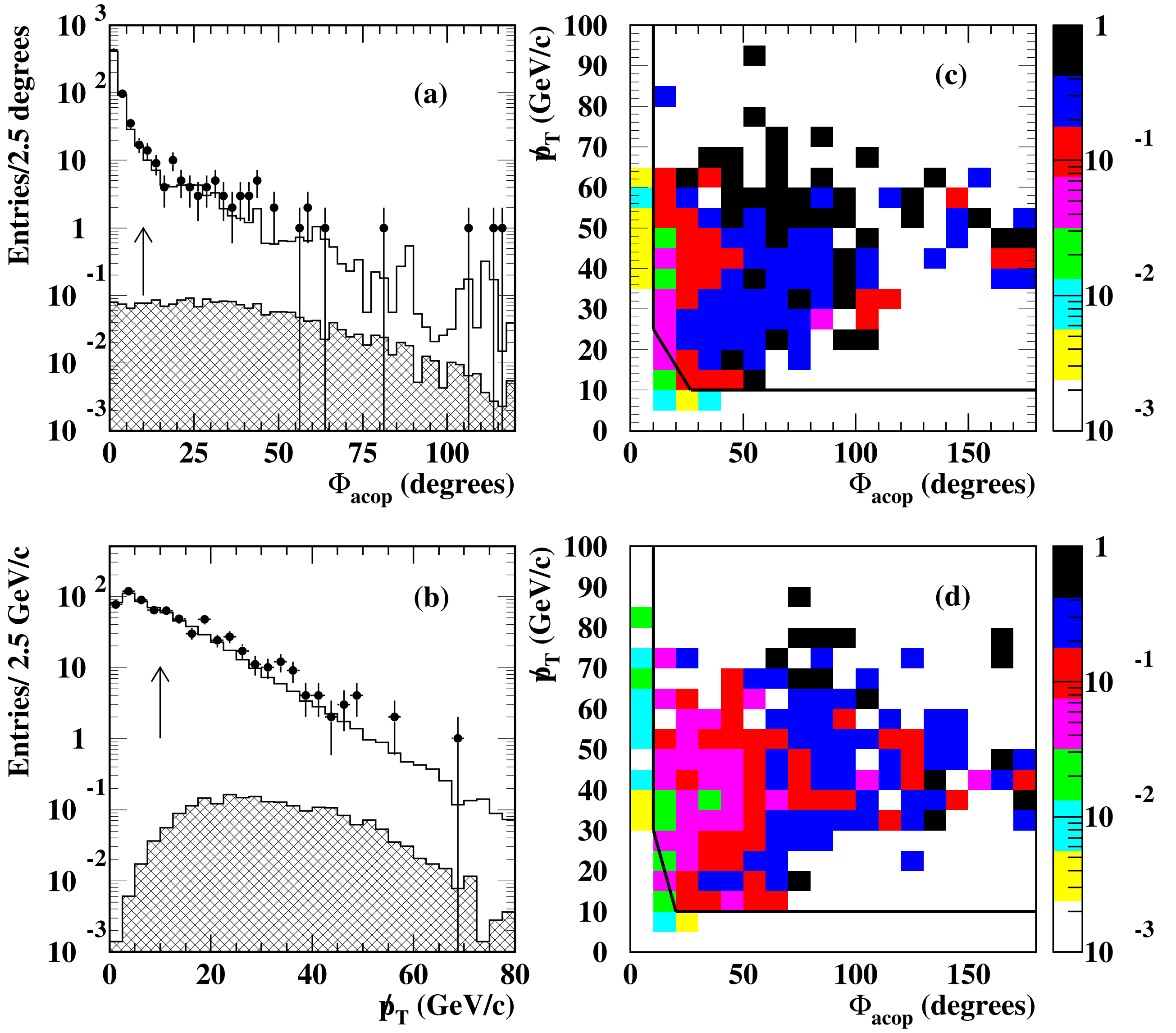

Figure 9: Acoplanarity (a) and missing transverse momentum (b) distribution for the Monte Carlo simulation (empty histogram) and the 1996 LEP2 data (full points). The contribution from the expected single W signal is shown as in the hatched histogram. The arrows indicate the position of the cuts. In (c) and (d) we show for $\sqrt{s} = 161$ and 172 GeV the ratio of the two dimensional Monte Carlo distributions for the signal and the background. The scale of the two dimensional plots is shown at the right. The events lying in the region to the left and below the thick lines are rejected in the analysis.

are found in the data. The efficiency for the signal is 46% and 51% respectively at $\sqrt{s} = 161$ and 172 GeV.

Since the remaining background is dominated by the $\mathrm{W^+W^-} \to \mathrm{q\overline{q}'}\ell\overline{\nu}_\ell$ decays we try to reject these events by identifying the lepton coming from the decay of one of the Ws. These leptons will be rather close in angle with the hadronic jets, since otherwise the events will not pass the y_{23} cut. To have high efficiency for the lepton identification we first check whether each charged track passes identification criteria best suited for a low multiplicity environment, and then we apply the standard high multiplicity lepton identification routines.

In the first case [25] electrons are identifyed by requiring a tight match between the measured ϕ coordinate of the track and electromagnetic cluster, by removing tracks consistent with photon conversions, and by requiring the ionisation energy loss, $\mathrm{d}E/\mathrm{d}x$, and the ratio of the electromagnetic cluster energy, E, to the track momentum, p, to be consistent with the expectation for an electron. A muon candidate is a track which has associated hits in the muon chambers or the hadron calorimeter, and has only a small energy deposit in the electromagnetic calorimeter. The electron idenfitication in a high multiplicity environment is based on a neural network [26], while the muon idenfitication [27] relies on the quality of the match between a track segment reconstructed in the muon chambers and the extrapolation of a track reconstructed in the central detector. A loose cut on $\mathrm{d}E/\mathrm{d}x$ is also used to reduce the kaon background.

In this way we can identify with high efficiency both the electrons and muons coming directely from the W decays, and also some of those coming from the chain decay $\mathrm{W} \to \tau \to (\mathrm{e}, \mu)$. Since the $\mathrm{W^+W^-} \to \mathrm{q\overline{q}'}\tau\overline{\nu}_\tau$ is then the largest background, we have used for $\sqrt{s} = 172$ GeV also the track(s) identified as τ decay products in the $\mathrm{W^+W^-} \to \mathrm{q\overline{q}'}\ell\overline{\nu}_\ell$ selection routines described in [22].

For each track identified as a lepton or as coming from the decay of a τ (for the 3-prong decay of the τ we construct a pseudo-track summing the momenta of the three tracks), we calculate the transverse momentum p_t^{lep} relative to the axis of the jet whom the track belongs to[6]. Hadrons misidentified as leptons and genuine leptons produced in the semileptonic decay $\mathrm{W} \to \mathrm{c\overline{s}} \to (\mathrm{e}, \mu)$ will have a low p_t^{lep}, contrary to the leptons being produced directely in the W decay. The distribution of the transverse momentum of the tracks identified as leptons is shown in figure 10. With a cut $p_t^{lep} \geq 3.0$ GeV/c (cut D) on the transverse momentum of these tracks the expected number of events is 2.2 (4.5) at $\sqrt{s} = 161(172)$ GeV, with a signal contribution of 0.7(1.0) events. Three events are observed in the data at $\sqrt{s} = 161$ GeV and six at 172 GeV. The remaining background is dominated by $\mathrm{W^+W^-} \to \mathrm{q\overline{q}'}\tau\overline{\nu}_\tau$ decays.

This background can be further reduced applying a cut on the missing longitudinal momentum. In the single W events the forward scattered electron carries a significant fraction of the beam momentum. Due to the presence of two or three neutrinos, the $\mathrm{W^+W^-} \to \mathrm{q\overline{q}'}\tau\overline{\nu}_\tau$ events should be instead more balanced along the beam direction. This cut on the missing longitudinal momentum should not be appliead on all the events, but rather only to those events where the transverse missing momentum is small. We find that an optimal cut uses the missing energy (cut E):

- $E_{miss} \geq 20.0$ GeV/c at $\sqrt{s} = 161$ GeV, and
- $E_{miss} \geq 35.0$ GeV/c at $\sqrt{s} = 172$ GeV.

The cut has to be raised, when moving away from the $\mathrm{W^+W^-}$ production threshold, due to the increased momentum of the W bosons. The distribution of the missing momentum is shown in figure 11, for the data and the simulation. After the above mentioned cut 3(3) events remain in the data at $\sqrt{s} = 161(172)$ GeV, against a prediction of 1.9 (2.5) events from the Monte Carlo, with a expected contribution of 0.65 (0.72) events coming from $\mathrm{e^+e^-} \to \mathrm{q\overline{q}'e}\overline{\nu}_\mathrm{e}$ satisfying the kinematical cuts defining the single W signal.

[6]Removing the track from the jet before computing the transverse momentum gives only a slight improvement in background rejection.

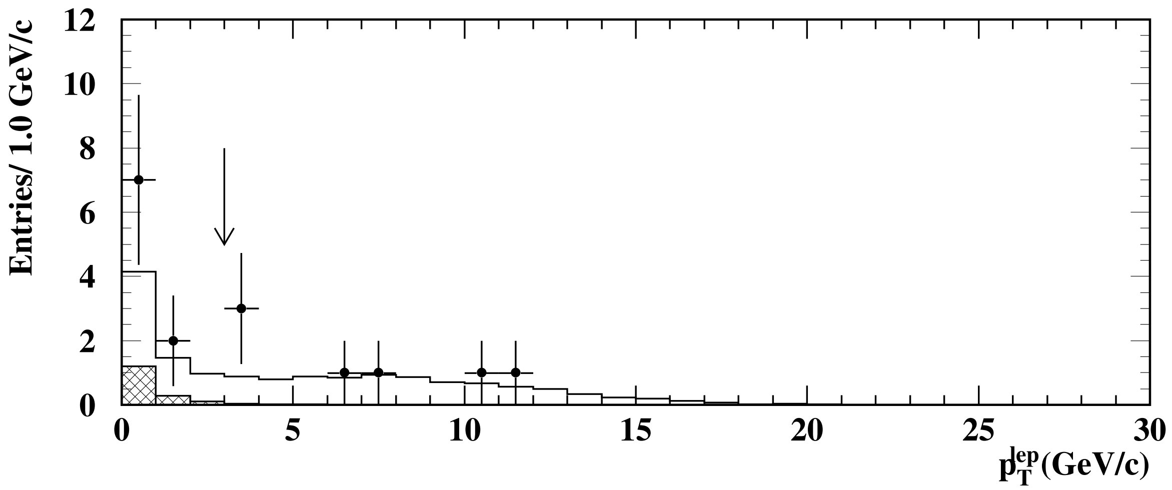

Figure 10: Distribution of the transverse momentum relative to the jet axis for the tracks identified as leptons. The empty histogram shows the distribution expected from the Monte Carlo simulation, and the full dots represent the 1996 LEP2 data points.The contribution from the expected single W signal is shown as in the hatched histogram. The arrow indicates the position of the cut.

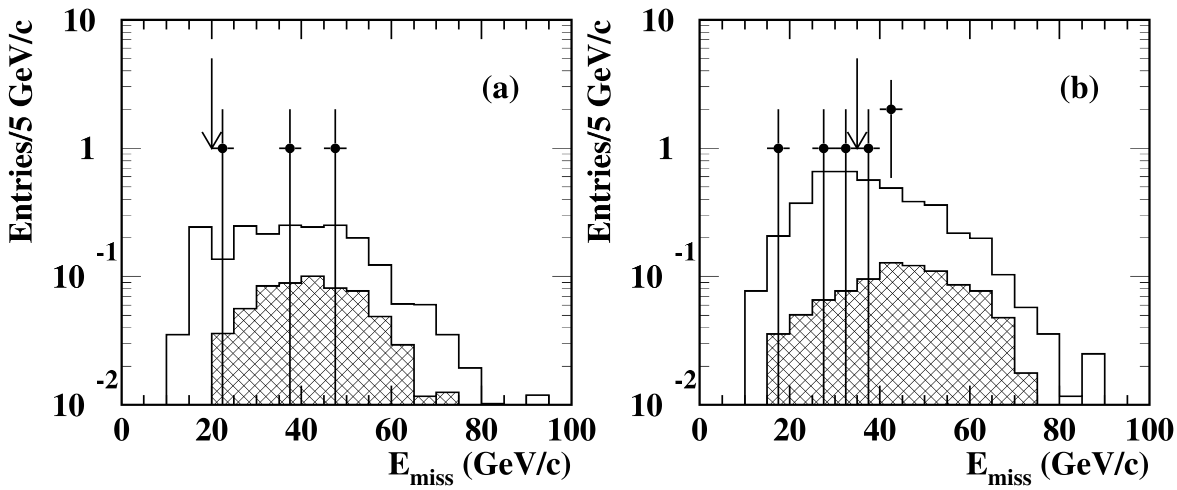

Figure 11: Distribution of the missing energy for $\sqrt{s}$ = 161 GeV (a) and 172 GeV (b).The empty histogram shows the distribution expected from the Monte Carlo simulation, and the full dots represent the 1996 LEP2 data points.The contribution from the expected single W signal is shown as hatched histogram. The arrows indicate the position of the cuts.

The invariant mass distribution of the events satisfying all cuts is shown in figure 12. The single W events appear as a peak in the distribution in the mass range 60-100 GeV/c^2, with a mass resolution of $\approx$ 10 GeV/c^2. In this signal region (cut F) we observe 2 events at $\sqrt{s}$ = 161 GeV and 2 events at $\sqrt{s}$ = 172 GeV, with an expectation of 1.1 and 1.4 events respectively. We give in appendix D the kinematical characteristics of the 4 candidate events, together with their pictures. The signal is expected to contribute for 0.62 and 0.64 events for the two center-of-mass energies. The remaining background is constituted mostly by $\mathrm{W^+W^-} \to \mathrm{q\overline{q}'}\tau\overline{\nu}_\tau$ events, with the τ decay giving low energy track(s) which are then merged inside one of the two jet coming from the hadronic decay of the W. Additional contribution to the background are given from $\mathrm{W^+W^-} \to \mathrm{q\overline{q}'e\overline{\nu}_e}$ and $\mathrm{W^+W^-} \to \mathrm{q\overline{q}'}\mu\overline{\nu}_\mu$ where the lepton is emitted in the forward direction, a region where the lepton identification criteria fail. A minor contribution is given from the $\mathrm{e^+e^-} \to \mathrm{q\overline{q}}$ events, while all the other backgrounds we have condidered are negligible.

The selection efficiencies, the number of selected in the Monte Carlo and in the LEP2 1996 data are summarised in table 4 and 5 for $\sqrt{s}$ = 161 and 172 GeV respectively. The dependency of the selection efficiency as a function of the anomalous couplings is shown in figure 13 and tabulated in Appendix E. We find that over the interesting range of values of κ_γ and of λ_γ the selection efficiency has a relative variation of 10 and 20% respectively, much larger than the 5% quoted as a systematic error due to this variation in [4]. It is therefore necessary to take into account the dependency of the selection efficiency when computing a limit on the cross section. The selection efficiency appears to increase when the couplings at the γWW vertex assume values different from the Standard Model one. This has the consequence that limits calculated assuming that the efficiency is constant will be conservative. The selection efficiency cannot be easily parametrised as a function of κ_γ and λ_γ, and for this reason we prefer to interpolate linearly between the points for which a full Monte Carlo simulation is available. We first assume that the relative variation of the selection efficiency can be calculated indipendently for the two couplings κ_γ and λ_γ and then perform a small correction, to take into account some correlation between them.

5 Systematic errors

Given that our expected signal to background ratio is approximately one, we need to estimate the systematic error both on the signal selection efficiency and on the accepted background cross section.

The only common systematic error for both signal and background comes from the luminosity measurement. The luminosity is determined with a statistical precision of 0.4% and a systematic error (which can be assumed to be correlated between the two center-of-mass energies) of 0.35% [28].

The following sources of systematic errors on the accepted background cross section are taken into account:

1. The 0.06 GeV error on the center-of-mass energies [14] causes a negligible error on the cross section for $\mathrm{e^+e^-} \to \mathrm{q\overline{q}}$ and a 0.25% error on the cross section for four fermion final states (assuming these are dominated by the $\mathrm{e^+e^-} \to \mathrm{W^+W^-}$ process).

2. The statistical error of the background Monte Carlo simulation is 6% and 4% at $\sqrt{s}$ = 161 and 172 GeV respectively.

3. We compare background predictions obtained with different Monte Carlo generators and use their difference as a systematic error. The difference between $\mathrm{e^+e^-} \to \mathrm{q\overline{q}}$ events generated with Pythia and Herwig introduces an error of 5% (dominated by the statistical uncertainty in the Monte Carlo samples). For the four fermion events the difference between `grc4f` and Excalibur amounts to 10% and 2% at $\sqrt{s}$ = 161 and 172 GeV respectively. Larger differences are observed between different two-photon Monte Carlo samples, but since no events are retained in the analysis procedure we neglect this systematic error.

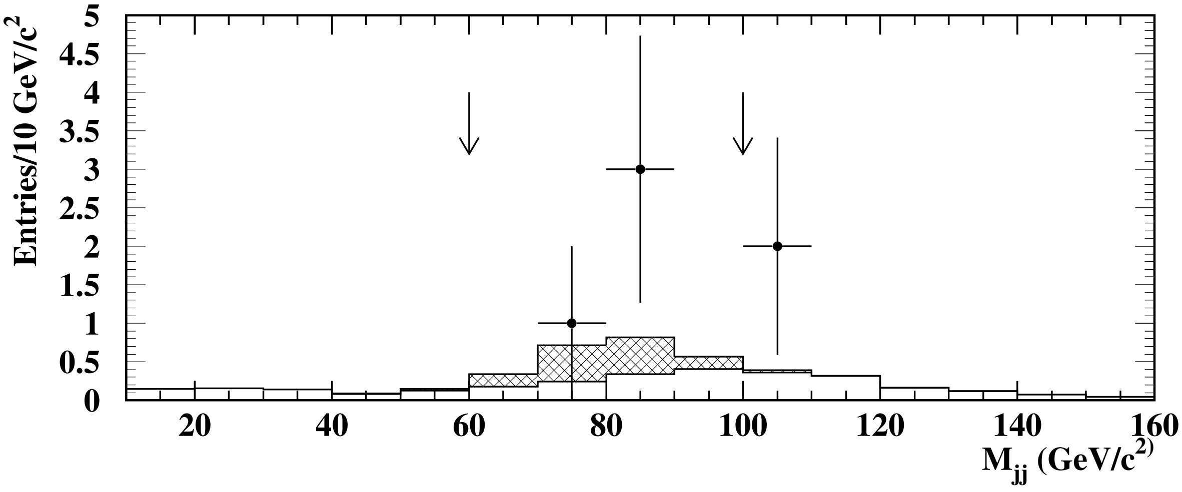

Figure 12: Distribution of the invariant mass of the two jet system. The empty histogram shows the distribution expected from the Monte Carlo simulation, and the full dots represent the 1996 LEP2 data points.The contribution from the expected single W signal is shown as in the hatched histogram. The arrows indicate the position of the cuts.

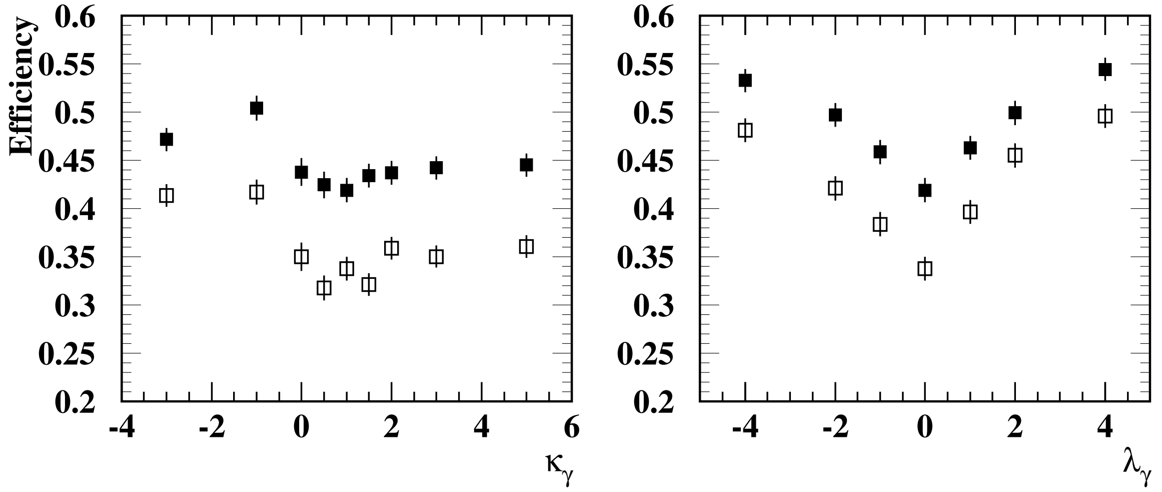

Figure 13: Selection efficiency for the simulated (using `grc4f` with the SF ISR method) single W events as a function of the anomalous couplings κ_γ and λ_γ for $\sqrt{s} = 161$ GeV (full dots - ■) and for $\sqrt{s} = 172$ GeV (empty dots - □). The error bars indicate the Monte Carlo statistical error.

161 GeV	$N_{\text{background}}$					N_{signal} $\mathrm{We}\overline{\nu}_{\mathrm{e}}$		ϵ_{signal} $\mathrm{We}\overline{\nu}_{\mathrm{e}}$		N_{data}
	$q\bar{q}$	4f	$\gamma\gamma$ unt.	$\gamma\gamma$ tag.	Σ_{BG}	(SF)	(PS)	(SF)	(PS)	
preselection	990 ± 3	31.3 ± 0.1	1390 ± 14	84 ± 3	2618 ± 15	1.16 ± 0.04	1.14 ± 0.04	78.4%	80.8%	2440
cut A	822 ± 3	25.2 ± 0.1	1048 ± 12	16 ± 1	1955 ± 13	1.08 ± 0.04	1.05 ± 0.04	73.2%	73.9%	1862
cut B	270 ± 1	9.1 ± 0.1	60 ± 3	1.0 ± 0.3	343 ± 3	0.90 ± 0.04	0.90 ± 0.04	61.7%	62.6%	379
cut C	0.43 ± 0.06	2.3 ± 0.05	0.1 ± 0.1	0	2.8 ± 0.2	0.67 ± 0.03	0.67 ± 0.03	47.7%	45.8%	6
cut D	0.33 ± 0.05	1.09 ± 0.03	0.1 ± 0.1	0	1.6 ± 0.2	0.65 ± 0.03	0.64 ± 0.03	46.7%	44.8%	3
cut E	0.28 ± 0.05	1.03 ± 0.03	0	0	1.31 ± 0.06	0.64 ± 0.03	0.62 ± 0.03	45.8%	43.5%	3
cut F	0.06 ± 0.02	0.45 ± 0.02	0	0	0.50 ± 0.03	0.61 ± 0.03	0.58 ± 0.03	44.0%	40.3%	2

Table 4: Expected events and selection efficiencies at $\sqrt{s} = 161$ GeV.

172 GeV	$N_{\text{background}}$					N_{signal} $\mathrm{We}\overline{\nu}_{\mathrm{e}}$		ϵ_{signal} $\mathrm{We}\overline{\nu}_{\mathrm{e}}$		N_{data}
	$q\bar{q}$	4f	$\gamma\gamma$ unt.	$\gamma\gamma$ tag.	Σ_{BG}	(SF)	(PS)	(SF)	(PS)	
preselection	854 ± 2	46.9 ± 0.2	1539 ± 17	104.14 ± 0.03	2544 ± 17	1.61 ± 0.05	1.61 ± 0.05	81.1%	79.2%	2661
cut A	702 ± 2	40.2 ± 0.2	1095 ± 15	19.53 ± 0.01	1858 ± 14	1.48 ± 0.05	1.43 ± 0.05	74.4%	70.4%	1971
cut B	225 ± 1	21.2 ± 0.2	56 ± 3	1.268 ± 0.003	304 ± 4	1.27 ± 0.05	1.21 ± 0.04	63.7%	59.6 %	329
cut C	0.66 ± 0.06	9.8 ± 0.1	0	0	10.5 ± 0.1	1.02 ± 0.04	0.98 ± 0.04	51.2%	48.3%	10
cut D	0.54 ± 0.06	2.94 ± 0.06	0	0	3.48 ± 0.09	0.95 ± 0.04	0.90 ± 0.04	48.0%	44.3%	6
cut E	0.23 ± 0.04	1.50 ± 0.04	0	0	1.73 ± 0.06	0.71 ± 0.03	0.63 ± 0.03	36.0%	31.0%	3
cut F	0.03 ± 0.01	0.68 ± 0.03	0	0	0.71 ± 0.03	0.68 ± 0.03	0.60 ± 0.03	34.1%	29.7%	2

Table 5: Expected events and selection efficiencies at $\sqrt{s} = 172$ GeV.

4. Any difference between the predicted and observed distributions of the variables used in the selection procedure is a source of uncertainty in the accepted background cross section. For each variable we use the normalised distribution of the data to reweight the background Monte Carlo samples in order to match the data. The resulting difference in the accepted cross section is then taken as systematic error. This procedure is applied to each variable in turn, taking two different data reference distributions. First we take as reference distribution that obtained prior to performing the cut on the considered variable, or just after cut B for the variables used in cuts C–F (we apply a looser preselection to study the multiplicity and the y_{23} cuts). To remove from the data the two photon events we also apply an invariant mass cut for the jet pair of 50 GeV/c^2. This results in a sample which is constituted for more than 90% by $\mathrm{e^+e^-} \rightarrow \mathrm{q\overline{q}}$ events. The second reference sample is enriched in four fermion events (reaching a fraction of 50% of the sample) by loosening the preselection cut to $y_{23} \leq 0.15$ and by requiring $\not{p}_t \geq 5.0$ GeV/c, $\phi_{\mathrm{acop}} \geq 5^\circ$, $|\cos\theta_{jj}| \leq 0.92$ and an invariant mass of the jet pair larger than 40 GeV/c^2. Comparable results are obtained with both methods, despite the limited data statistic available. The systematic error obtained with this procedure for each variable used in the selection is shown in table 6. Summing all the different errors in quadrature we obtain a systematic error of 7.5%.

5. The effect of ignoring the dependency of the accepted background cross section from the anomalous couplings κ_γ and λ_γ is discussed in section 6.

Summing in quadrature all the different errors we obtain a total error on the background prediction of 15% and 10% at $\sqrt{s} = 161$ and 172 GeV respectively.

Variable used in the selection	Relative variation of the background
Track multiplicity	1.0%
Cluster multiplicity	0.5%
y_{23}	4.5%
$\mathrm{E_{GC}}$, $\mathrm{E_{FD}}$, $\mathrm{E_{SW}}$	2.0%
$\lvert\cos\theta_{j_{1,2}}\rvert$, $\lvert\cos\theta_{jj}\rvert$	2.5%
ϕ_{acop}	0.5%
$\not{p}_t$	1.0%
p_t^{lep}	1.5%
E_{miss}	2.5%
Invariant mass cut	3.5%
Total	7.5%

Table 6: Systematic errors for the background description.

For the signal we take into account the following sources of systematic errors:

1. The Monte Carlo statistics causes an uncertainty of 3% in the selection efficiency.

2. The difference between the two methods available in `grc4f` for generating the initial state radiation, causes an uncertainty of 5% in the selection efficiency, and an uncertainty of 3% in the absolute cross section.

3. The cross section of the single W process is computed with α_{em} fixed at $Q^2 = 0$. Ignoring the running of α_{em} in the range of Q^2 0–0.2 (GeV/c)^2 is equivalent to underestimating the cross section for at most 1.5%, which we take as additional systematic error.

4. The extrapolation of the signal detection efficiency as a function of the anomalous couplings κ_γ and λ_γ causes an uncertainty of 5%.

5. The mean charged track and electromagnetic calorimeter cluster multiplicity of the Monte Carlo signal sample agree within errors with those measured in the data using a sample of $W^+W^- \to q\overline{q}'\ell\overline{\nu}_\ell$ decays identified as in [22]. Variation of the mean charged track multiplity of one unit and of the electromagnetic cluster multiplicity of two units result in a systematic uncertainty of 0.7%.

6. The cut on the jet recombination parameter $y_{23} \leq 0.03$ introduces an inefficiency of $8.7 \pm 1.0\%$. When $W^+W^- \to q\overline{q}'\ell\overline{\nu}_\ell$ decays identified as in [22] are considered, removing the lepton from the event, this cut introduces an inefficiency of $7.8 \pm 4.0\%$. The two results being compatible, the statistical uncertainty of the latter is taken as systematic error.

7. Additional energy deposits in the forward calorimeters due to beam halo may cause a reduction of the signal selection efficiency. We shift in the Monte Carlo samples the energy measured in the forward calorimeters by the difference between the average deposits in the data and in the simulation. We then take the change in the selection efficiency of the single W signal (2%) as systematic error.

8. Differences between the reconstructed jet angles in Z^0 data collected in 1996 prior to the high energy runs and Monte Carlo simulations are discussed in [29, 30]. The simulation describes correctly the resolution on the jet angles, although a shift in the polar angle of less than $0.5°$ is observed. The effect of changing the polar angle of the jets alone or of the reconstructed two jet system by this quantity introduces an uncertainty on the signal selection efficiency of 2%. Applying the same shift to the azimuthal angle (and thus to the acoplanarity of the jet pair) results in a systematic uncertainty of 1%.

9. Analogously the Monte Carlo simulation is found to reproduce correctly the distribution of the missing transverse momentum, as shown in figure 9b. If the missing transverse momentum and the missing energy are shifted in the signal Monte Carlo for the the difference in the mean values of distributions between data and background Monte Carlo samples (respectively by 0.5 GeV/c and by 1.0 GeV), the selection efficiency of the signal changes by 2.5% which we take as systematic error.

10. The efficiency of the cut on the transverse momentum of the tracks identified as leptons has been studied using $W^+W^- \to q\overline{q}'q\overline{q}'$ decays selected as in [22], ignoring possible differences in the angular distribution and in the spectra of W bosons. This cut removes $8.5 \pm 3.8\%$ of the events, whereas the single W Monte Carlo gives an inefficiency of $5.0 \pm 0.7\%$. Taking into account that in the first case two W bosons contribute to the inefficiency, the two results are compatible, and we take the statistical error of the data efficiency (2%) as systematic error.

11. The effect of the cut on the invariant mass of the jet pair can be checked using radiative returns to the Z^0 peak. The position of the peak is shifted in the data by -0.6 ± 1.0 GeV relative to that of the Monte Carlo, and the mass resolution is a factor $11 \pm 11\%$ worse in the Monte Carlo than in the data (similar results are obtained in [31]). If the shift is applied in the Monte Carlo, and the smearing of the W mass peak due to the reconstruction is worsened by the factor derived above, the selection efficiency of the single W signal changes by 2.5%, which we take as systematic error.

12. The systematic error due to the uncertainty on the trigger efficiency is assumed to be negligible, because of the high track multiplicity requirement.

13. Uncertainties related to the fragmentation process are estimated to be smaller than 2% by comparing the difference between the selection efficiencies obtained by fragmenting the same four-fermion final state with JETSET and with HERWIG.

Summing all these contributions in quadrature we obtain a systematic error on the single W selection efficiency of 10%.

6 Limit on the anomalous couplings

As shown in section 2 the cross section for the single W process has a quadratic dependence on the anomalous couplings κ_γ and λ_γ. We obtain limits on these parameters by performing a maximum likelihood fit to the number of observed events. We perform the fit assuming that only the single W cross section varies if the anomalous couplings assume values different from the Standard Model predictions. This is clearly not the case, being the background dominated by the $e^+e^- \to W^+W^-$ process, which also depends on anomalous TGCs. It is however an assumption which leads to conservative limits, which are independent (at the level of 3% as shown in section 2) from the relation between the couplings at the γWW and at the Z^0WW vertices.

If the $e^+e^- \to W^+W^-$ background were only a small fraction of the signal, or if the deviation of its cross section from the Standard Model value was much slower than that of the single W process, it would be possible to incorporate possible deviations of the background cross section from the Standard Model value into the background systematic error. Assuming then that all the dependency from anomalous TGCs is in the signal cross section (and selection efficiency), the final fit results would not deviate considerably from that obtained when the fit is performed allowing for both the signal and the background cross section to depend on the anomalous TGCs.

Unfortunately in our case the signal to background ratio is approximately one and relative deviation of the signal and the background cross section from the Standard Model values in presence of anomalous TGCs is of the same magnitude. This would indicate the necessity of a fit which allows for both the signal and the background cross sections to vary, which then require that some assumptions are made about the relations among the γWW and Z^0WW couplings (i.e. choosing one of the models indicated in section 2).

Assuming instead that the dependency from anomalous TGCs is contained only in the signal cross section, gives a conservative limit independent from the couplings at the Z^0WW vertex. This second approach can be pursued only as long as no lower limit on the cross section can be set. The single W cross section goes through a minimum for $\kappa_\gamma = 0$ and a measurement of the cross section alone would then give boundaries only for $|\kappa_\gamma|$. If the dependency of the background from TGCs were ignored, the lower bound on $|\kappa_\gamma|$ would be shifted to larger values. This is not found to be a problem with the current level of statistics, as shown below.

The problem of including the background dependency on TGCs in the fit will disappear as soon as it will be possible to fit the W mass peak in the selected sample. Due to the presence of the τ decay products the invariant mass of the two jet system in background events peaks at values larger than the W mass. The number of signal events could then be derived from the fit to the mass distribution, irrespective of the values of the couplings in the $e^+e^- \to W^+W^-$ process, provided that these do not change the shape of the background.

We choose the conservative approach of allowing for anomalous TGCs only in the signal cross section because of its simplicity and since it retains the property that the limit obtained is independent from the couplings at the Z^0WW vertex. Without considering the errors on the signal selection efficiency and on the accepted background cross section, we would simply maximise the product of the Poisson probabilities to observe 2 events at $\sqrt{s} = 161$ GeV and 2 events at $\sqrt{s} = 172$ GeV. To include the systematic errors we allow the number of expected signal and background events to vary according to a gaussian distributions with widths corresponding to the estimated errors. We then maximise the integral of the product of the two Poisson probabilities and of the gaussian functions introduced to represent the systematic errors.

Care should be taken to treat differently the systematic errors which are common between signal and background, or between samples taken at different energies. Since the integration is performed numerically, we try to keep the fit simple, and for this reason we introduce only three gaussian curves: two for the background and one for the signal. This is justified, since the error for the background at $\sqrt{s} = 161$ GeV has a large component coming from the Monte Carlo statistics, which is not the case at $\sqrt{s} = 172$ GeV. For the signal instead the errors between the two center-of-mass energies can be assumed to be fully correlated.

The results of two fits (without and including the systematic errors) are shown in figure 14. The inclusion of the systematic errors induces a negligible effect on the limits which are obtained. The cross section for the $\mathrm{e^+e^-} \to \mathrm{q\overline{q}'e\overline{\nu}_e}$ process in the kinematic region we use to define the single W signal is found to be smaller than 0.85 pb and 1.2 pb at the 95% confidence level for $\sqrt{s} = 161$ and 172 GeV respectively.

From the likelihood curves the following limits at the 95% confidence level on the anomalous couplings are derived:

$$\begin{aligned} -3.2 \leq \ & \kappa_\gamma \ \leq 3.2 \\ -4.0 \leq \ & \lambda_\gamma \ \leq 4.1 \end{aligned}$$

A small region around $\kappa_\gamma = 0$ is excluded at the 68% confidence level, but as discussed above, this is an effect of the assumption of neglecting the TGC dependence of the accepted background cross section.

Under the assumption that $\alpha_{W\phi} = 0$ these limits can be converted into the following 95% confidence level limits for the α parameters:

$$\begin{aligned} -4.2 \leq \ & \alpha_{B\phi} \ \leq 2.2 \\ -4.0 \leq \ & \alpha_W \ \leq 4.1 \end{aligned}$$

7 Conclusions

We have isolated a sample of 4 events at $\sqrt{s} = 161 - 172$ GeV compatible with the $\mathrm{e^+e^-} \to \mathrm{q\overline{q}'e\overline{\nu}_e}$ process in the kinematic region dominated by the single W process. From a fit of the cross section as a function of the anomalous couplings at the γWW vertex we derive the 95% confidence level limits $-3.2 \leq \kappa_\gamma \leq 3.2$ and $-4.0 \leq \lambda_\gamma \leq 4.1$, compatible with those reported from the L3 Collaboration [4].

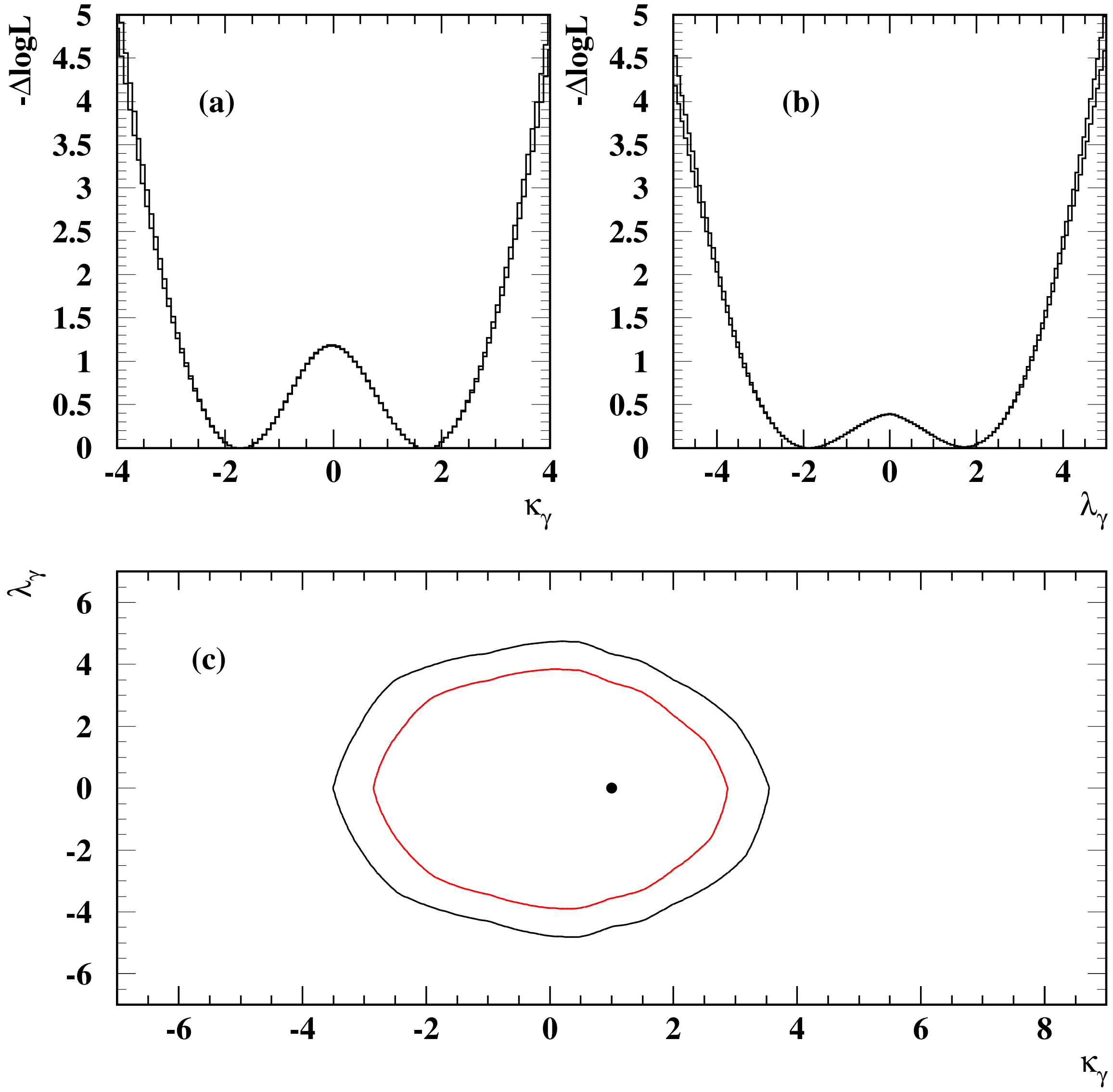

Figure 14: Difference of the log-likelihood relative to the maximum found by the fit as a function of κ_γ for $\lambda_\gamma = 0$ (a) and λ_γ for $\kappa_\gamma = 1$ b). The upper curve and lower curve show the result of the fit neglecting and including the systematic errors. The black line and the dark grey line in (c) indicate respectively the exclusion regions at the 95% and 70% confidence level in the parameter space (κ_γ,λ_γ). The point shows the expected value of the γWW couplings in the Standard Model.

References

[1] Physics at LEP2, Edited by G. Altarelli, T. Sjostrand and F. Zwirner, Report on the LEP2 Workshop 1995, CERN 96-01, Vol. 1, p. 525.

[2] C.G. Papadopoulos, Phys. Lett. **B333** (1994) 202.

[3] T. Tsukamoto and Y. Kurihara, Phys. Lett. **B389** (1996) 162.

[4] L3 Collaboration, M. Acciarri *et al.*, Phys. Lett. **B403** (1997) 168.

[5] K. Hagiwara, H. Iwasaki, A. Miyamoto, H. Murayama and D. Zeppenfeld, Nucl. Phys. **B365** (1994) 544.

[6] J. Fujimoto *et al.*, Comp. Phys. Comm. **100** (1997) 128.

[7] K. Hagiwara, R.D. Peccei, D. Zeppenfeld and K. Hikasa, Phys. Lett. **B282** (1987) 353,
M. Bilenky, J.L. Kneur, F.M. Renard and D. Schildknecht, Nucl. Phys. **B409** (1993) 22, Nucl. Phys. **B419** (1994) 240.

[8] CDF Collaboration, F. Abe *et al.*, Phys. Rev. Lett. **74** (1995) 1936, Phys. Rev. Lett. **75** (1995) 1017, Phys. Rev. Lett. **78** (1997) 4536,
D0 Collaboration, S. Abachi *et al.*, Phys. Rev. Lett. **78** (1997) 3634, *Studies of gauge boson pair production and trilinear couplings*, preprint Fermilab-Pub-97/088-E, hep-ex/9704004.

[9] The OPAL Collaboration, K. Ackerstaff *et al.*, Phys. Lett. **B397** (1997) 147, The OPAL Collaboration,, *Measurement of triple gauge boson couplings from* $\mathrm{W^+W^-}$ *production at* $\sqrt{s} = 172$ *GeV*, OPAL Physics Note PN287, March 1997.

[10] C.G. Papadopoulos, Comp. Phys. Comm. **101** (1997) 183.

[11] F.A. Berends, R. Pittau and R. Kleiss, Comp. Phys. Comm. **85** (1995) 437; the latest version (3.0) of the program is used.

[12] F.A. Berends, R. Pittau and R. Kleiss, Nucl. Phys. **B424** (1994) 308.

[13] M. Skrzypek, S. Jadach, W. Placzek and Z. Was, Comp. Phys. Comm. **94** (1996) 216, version 1.31 or 1.33 of KORALW incorporating the `grc4f` matrix elements.

[14] LEP Energy Working Group, private communication, January 1997.

[15] T. Sjöstrand, Comp. Phys. Comm. **82** (1994) 74.

[16] G. Marchesini *et al.*, Comp. Phys. Comm. **67** (1992) 465.

[17] D. Bardin et al., CERN-TH 6443/92 (May 1992); Phys. Lett. **B255** (1991) 290; Nucl. Phys. **B351** (1991) 1; Zeit. Phys. **C44** (1989) 493. We use ZFITTER version 5.0 with default parameters, except `BOXD`=1, `CONV`=1, `INTF`=0 and `FINR`=0, and with the following input parameters: $M_{\mathrm{Z}^0} = 91.1863$ GeV, $M_{\mathrm{top}} = 175$ GeV, $M_{\mathrm{Higgs}} = 300$ GeV, $\alpha_{\mathrm{em}}(M_{\mathrm{Z}^0}) = 1/128.896$, $\alpha_{\mathrm{s}}(M_{\mathrm{Z}^0}) = 0.118$.

[18] R. Engel and J. Ranft, Phys. Rev. **D54** (1996) 4244, R. Engel, Zeit. Phys. **C66** (1995) 203.

[19] A. Buijs, W. G. J. Langeveld, M. H. Lehto and D. J. Miller, Comp. Phys. Comm. **79** (1994) 523.

[20] J. Hilgart, R. Kleiss and F. Le Diberder, Comp. Phys. Comm. **75** (1993) 191.

[21] M. Kobel, private communication and *How to make a complete 4-fermion Monte Carlo sample,* `http://opalinfo.cern.ch/opal/group/smproc/4fermion.txt`.

[22] The OPAL Collaboration,, *Production of* $\mathrm{W^+W^-}$ *in* $\mathrm{e^+e^-}$ *collisions at* $\sqrt{s} = 172$ *GeV*, OPAL Physics Note PN273, January 1997.

[23] N. Brown and W.J. Stirling, Phys. Lett. **B252** (1990) 657;
S. Bethke, Z. Kunszt, D. Soper and W.J. Stirling, Nucl. Phys. **B370** (1992) 310;
S. Catani *et al.*, Phys. Lett. **B269** (1991) 432;
N. Brown and W.J. Stirling, Zeit. Phys. **C53** (1992) 629.

[24] The OPAL Collaboration, M.Z. Akrawy *et al.*, Phys. Lett. **B253** (1990) 511.

[25] The OPAL Collaboration, K. Ackerstaff *et al.*, Phys. Lett. **B389** (1996) 416.

[26] The OPAL Collaboration, R. Akers *et al.*, Zeit. Phys. **C70** (1996) 357.

[27] The OPAL Collaboration, R. Akers *et al.*, Zeit. Phys. **C65** (1995) 17.

[28] The OPAL Collaboration, R. Akers *et al.*, *Tests of the standard and constraints on new physics from measurement of fermion pair production at 130-172 GeV at LEP*, preprint CERN-PPE/97-xxx in preparation.

[29] C.P. Ward and D.R. Ward, *A simple measurent of the mass of W boson by direct reconstruction*, OPAL Technical Note TN461, February 1997.

[30] D.R. Ward, *Separation of non radiative* $\mathrm{Z^0}/\gamma \to \mathrm{q\overline{q}}$ *events at LEP2*, OPAL Technical Note TN394, July 1996.

[31] E. Duchovni, D. Lellouch, G. Mikenberg and T. Wlodek, GCE++: *an algorithm for event energy measurement*, OPAL Technical Note TN306, June 1995.

Appendix A `grc4f` data cards

The signal Monte Carlo is generated using `grc4f` version 1.2 with the following data cards:

```
process=eNEuD    or eNEcS
scheme=gmu
energy=161.0d0   or 172.0d0
type=sf          or qedpsi
canon=no
coulomb=yes
qcdcr=yes
gluon=no
amw=80.33d0
agw=2.085d0
amz=91.1887d0
agz=2.4973d0
alphai=137.036d0
alpha_s=0.120d0
itmx=14,20
acc=0.1,0.05
ncall=160000
cernlib=yes
hadron=yes
qcd_shower=yes
thecut3=11.478341d0,0.d0
thecut5=168.521659d0,11.478341d0
thecut6=168.521659d0,11.478341d0
end
```

Appendix B Single W cross sections

The $e^+e^- \to q\overline{q}' e\overline{\nu}_e$ cross sections calculated with `grc4f` are given in table 7 for $\sqrt{s} = 161$ and 172 GeV as a function of the anomalous couplings κ_γ and λ_γ, for the two treatments of the initial state radiation (SF and PS).

κ_γ	λ_γ	$\sqrt{s} = 161$ GeV		$\sqrt{s} = 172$ GeV	
		σ_{SF} (fb)	σ_{PS} (fb)	σ_{SF} (fb)	σ_{PS} (fb)
1.00	0.00	145.5±0.7	141.5±0.7	191.8±1.0	188.6±1.0
1.25	0.00	195.4±0.8	189.5±0.8	258.3±1.2	251.7±1.2
1.50	0.00	256.3±1.0	248.3±1.0	332.4±1.5	326.8±1.5
2.00	0.00	404.9±1.5	398.7±1.5	514.1±2.2	515.3±2.2
3.00	0.00	821.9±2.9	814.1±2.9	1054.2±4.1	1039.7±4.1
5.00	0.00	2142.6±7.4	2138.6±7.3	2726.8±9.0	2714.6±9.0
0.75	0.00	106.3±0.5	102.4±0.5	142.8±0.8	138.2±0.8
0.50	0.00	77.4±0.4	73.4±0.4	106.3±0.6	102.4±0.6
0.00	0.00	49.4±0.3	46.7±0.3	70.0±0.5	68.1±0.5
-1.00	0.00	120.9±0.6	116.9±0.6	157.6±0.9	153.2±0.9
-3.00	0.00	746.1±2.8	737.9±2.8	938.3±3.9	935.0±3.9
1.00	1.00	183.9±0.8	179.4±0.8	245.1±1.2	242.4±1.2
1.00	2.00	292.2±1.3	286.1±1.3	391.9±2.0	390.4±2.0
1.00	4.00	715.9±3.1	720.4±3.1	977.3±4.9	971.2±4.9
1.00	-1.00	179.6±0.8	173.3±0.8	238.6±1.2	233.9±1.2
1.00	-2.00	281.1±1.2	277.0±1.2	377.5±1.9	375.4±1.9
1.00	-4.00	700.8±3.0	696.5±3.0	944.7±4.8	948.7±4.7
2.00	1.00	445.1±1.7	442.5±1.7	574.7±2.4	573.1±2.4
0.00	1.00	85.1±0.5	81.5±0.5	117.8±0.7	116.3±0.7
2.00	-1.00	429.8±1.7	426.3±1.7	565.2±2.4	557.4±2.4
0.00	-1.00	88.7±0.5	85.1±0.5	119.3±0.7	115.4±0.7
3.00	2.00	983.3±3.5	980.6±3.5	1268.7±5.0	1258.1±5.1
3.00	-2.00	943.7±3.5	934.0±3.5	1213.5±5.1	1218.4±5.0
-1.00	2.00	252.3±1.2	250.1±1.2	341.0±1.9	337.4±1.9
-1.00	-2.00	280.1±1.2	273.4±1.2	359.4±1.8	357.1±1.8

Table 7: Single W cross section as function of the anomalous couplings κ_γ and λ_γ. The Standard Model cross section are obtained for $\kappa_\gamma = 1$ and $\lambda_\gamma = 0$.

Appendix C List of Monte Carlo runs

The list of Monte Carlo runs, and their equivalent luminosity, which have been used for simulating the backgrounds is shown in table 8 for $\sqrt{s} = 161$ and 172 GeV. The possible alternatives to produce a complete four fermion background are then indicated in figure 15. The basic difference lies in the treatment of the $e^+e^-q\overline{q}$ final state. In one case different Monte Carlo samples are added, based on the different types of diagrams (multiperipheral, annihilation and conversion), whereas in the second case all Monte Carlo samples are added up, and double counting is avoided by performing angular cuts at the fermion level.

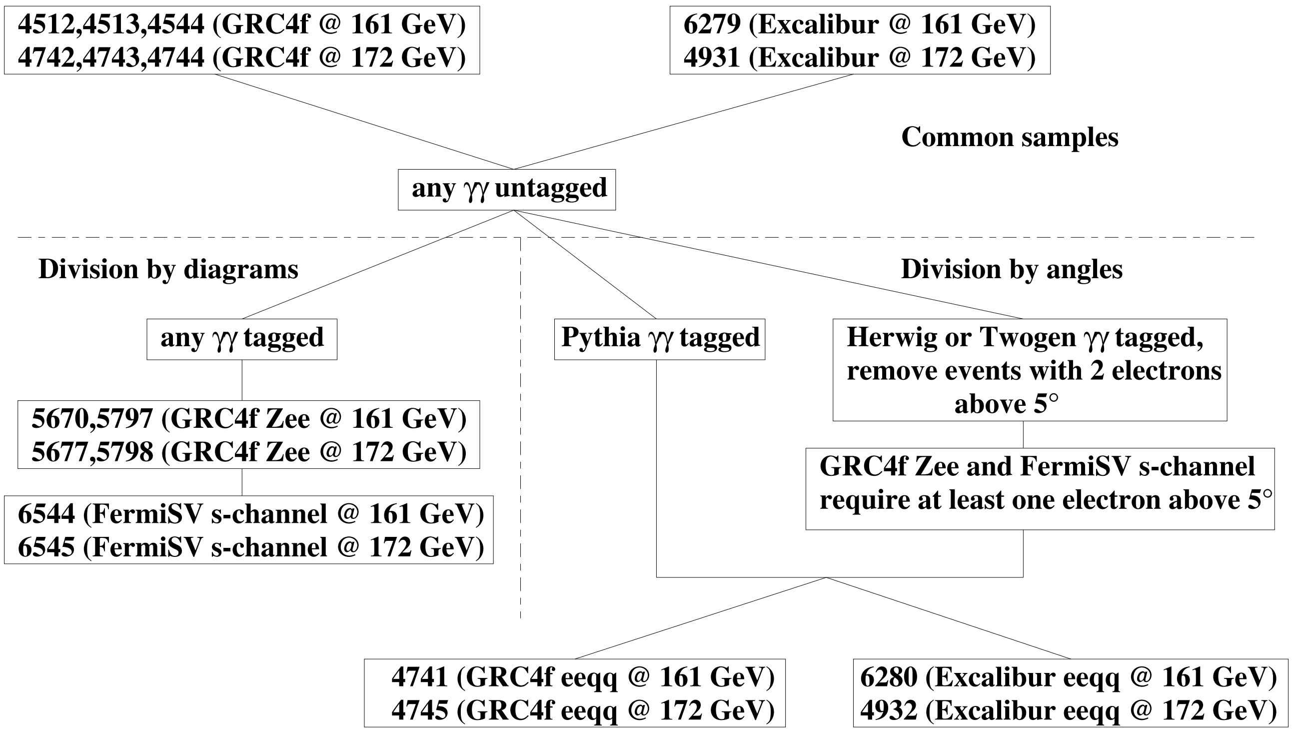

Figure 15: Flow chart indicating the possible alternatives for building a complete four fermion background Monte Carlo sample. The dashed line separates the samples common betwee the different approaches, and the two way of avoiding the double counting of the $e^+e^-q\overline{q}$ final states.

Run numbers	Generator	Number of events	Equivalent $\mathcal{L}$
$\sqrt{s} = 161$ GeV			
$e^+e^- \to q\overline{q}$			
4419	PYTHIA	200000	1357 pb^{-1}
1115	HERWIG	69000	459 pb^{-1}
High Q^2 (tagged) $\gamma\gamma \to had$			
1722	HERWIG	100000	104 pb^{-1}
1760	TWOGEN	50000	50 pb^{-1}
1723	PYTHIA	100000	144 pb^{-1}
Low Q^2 (untagged) $\gamma\gamma \to had$			
1719	PHOJET	999999	70 pb^{-1}
1725	PYTHIA	999999	56 pb^{-1}
General four fermion samples - excluding $e^+e^-q\overline{q}$ final states			
4512,4513,4544	`grc4f`	24000	$\approx$ 4000 pb^{-1}
6279	EXCALIBUR	60000	10147 pb^{-1}
Four fermion samples - $e^+e^-q\overline{q}$ final states			
4741	`grc4f`	25000	4844 pb^{-1}
6280	EXCALIBUR	120000	10591 pb^{-1}
Special four fermion samples - *s-channel* $e^+e^-q\overline{q}$			
6544	FERMISV	3460	5600 pb^{-1}
Special four fermion samples - $e^+e^- \to Z^0e^+e^-$			
5670,5797	`grc4f`	47689	$\approx$ 500 pb^{-1}
$\sqrt{s} = 172$ GeV			
$e^+e^- \to q\overline{q}$			
5035	PYTHIA	200000	1653 pb^{-1}
1119	HERWIG	100000	815 pb^{-1}
High Q^2 (tagged) $\gamma\gamma \to had$			
1120	HERWIG	100000	120 pb^{-1}
1770	TWOGEN	50000	48 pb^{-1}
1763	PYTHIA	100000	138 pb^{-1}
Low Q^2 (untagged) $\gamma\gamma \to had$			
1767	PHOJET	999999	50 pb^{-1}
1762,1783	PYTHIA	1204043	73 pb^{-1}
General four fermion samples - excluding $e^+e^-q\overline{q}$ final states			
4742,4743,4744	`grc4f`	74569	5000 pb^{-1}
4931	EXCALIBUR	100000	7528 pb^{-1}
Four fermion samples - $e^+e^-q\overline{q}$ final states			
4745	`grc4f`	23649	5000 pb^{-1}
4932	EXCALIBUR	70000	7980 pb^{-1}
Special four fermion samples - *s-channel* $e^+e^-q\overline{q}$			
6545	FERMISV	5610	5000 pb^{-1}
Special four fermion samples - $e^+e^- \to Z^0e^+e^-$			
5670,5797	`grc4f`	47411	500 pb^{-1}

Table 8: Monte Carlo samples used for simulating the background.

Appendix D Properties of selected events

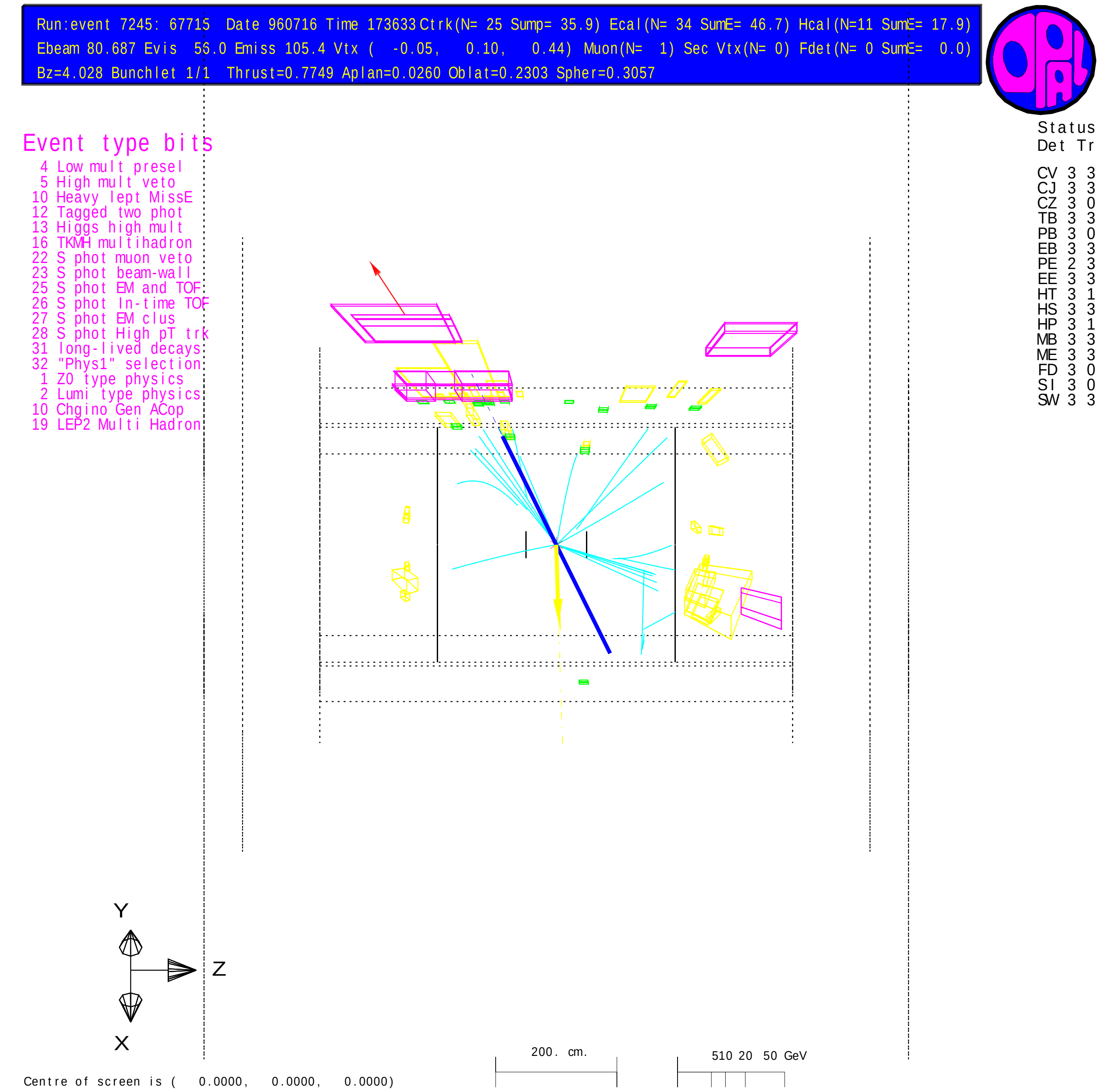

Figure 16: Third selected event: run 7245, event 67715, $\sqrt{s} = 161$ GeV, $\not{p}_t = 32.2$ GeV/c, $\phi_{\rm acop} = 42.8°$, $E_{miss} = 36.5$ GeV, $M_{\rm q\bar{q}'} = 83.3$ GeV/c^2.

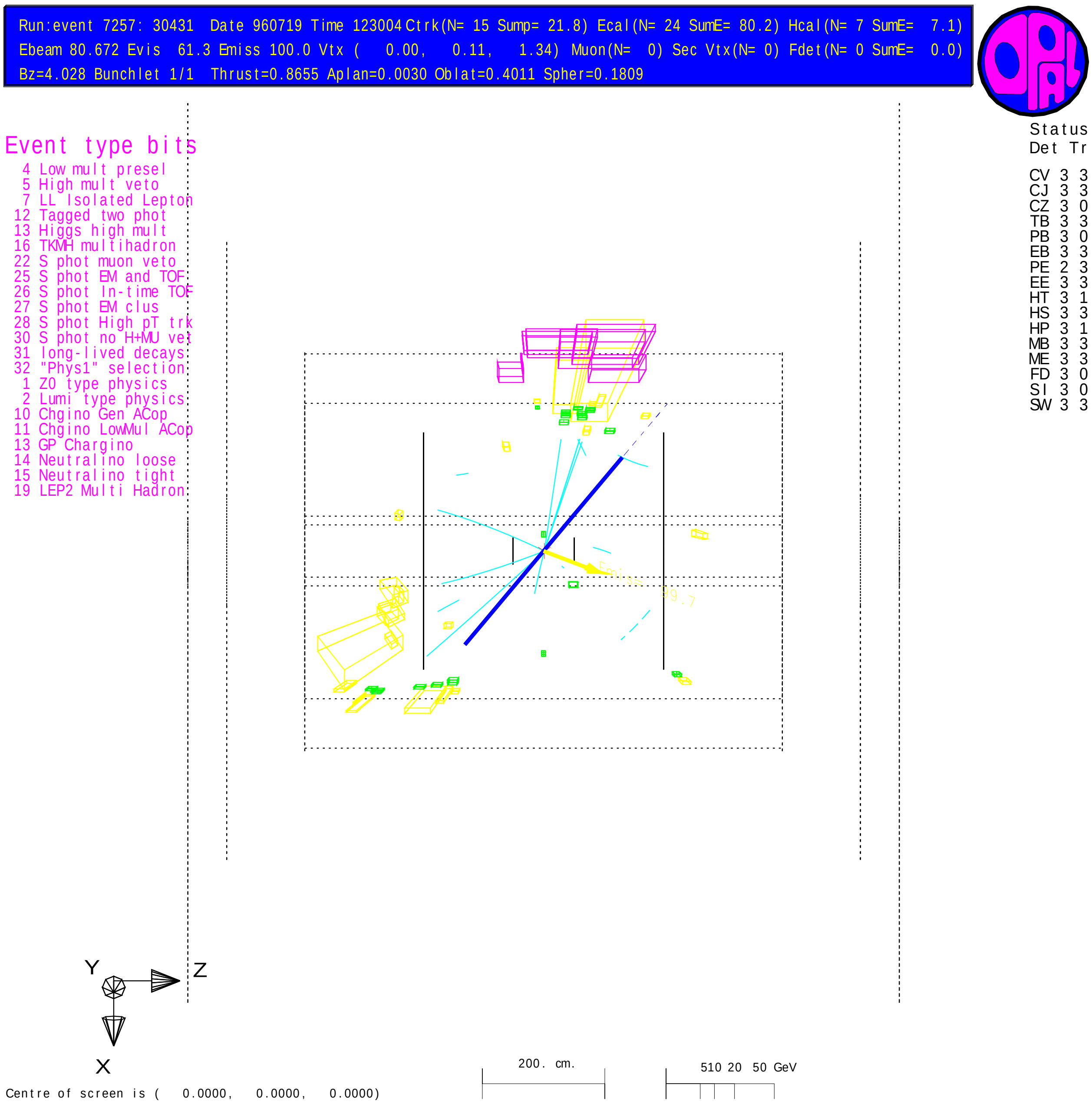

Figure 17: Second selected event: run 7257, event 30341, $\sqrt{s} = 161$ GeV, $\not{p}_t = 47.3$ GeV/c, $\phi_{\mathrm{acop}} = 48.8°$, $E_{miss} = 49.5$ GeV, $M_{\mathrm{q\bar{q}'}} = 79.8$ GeV/c^2.

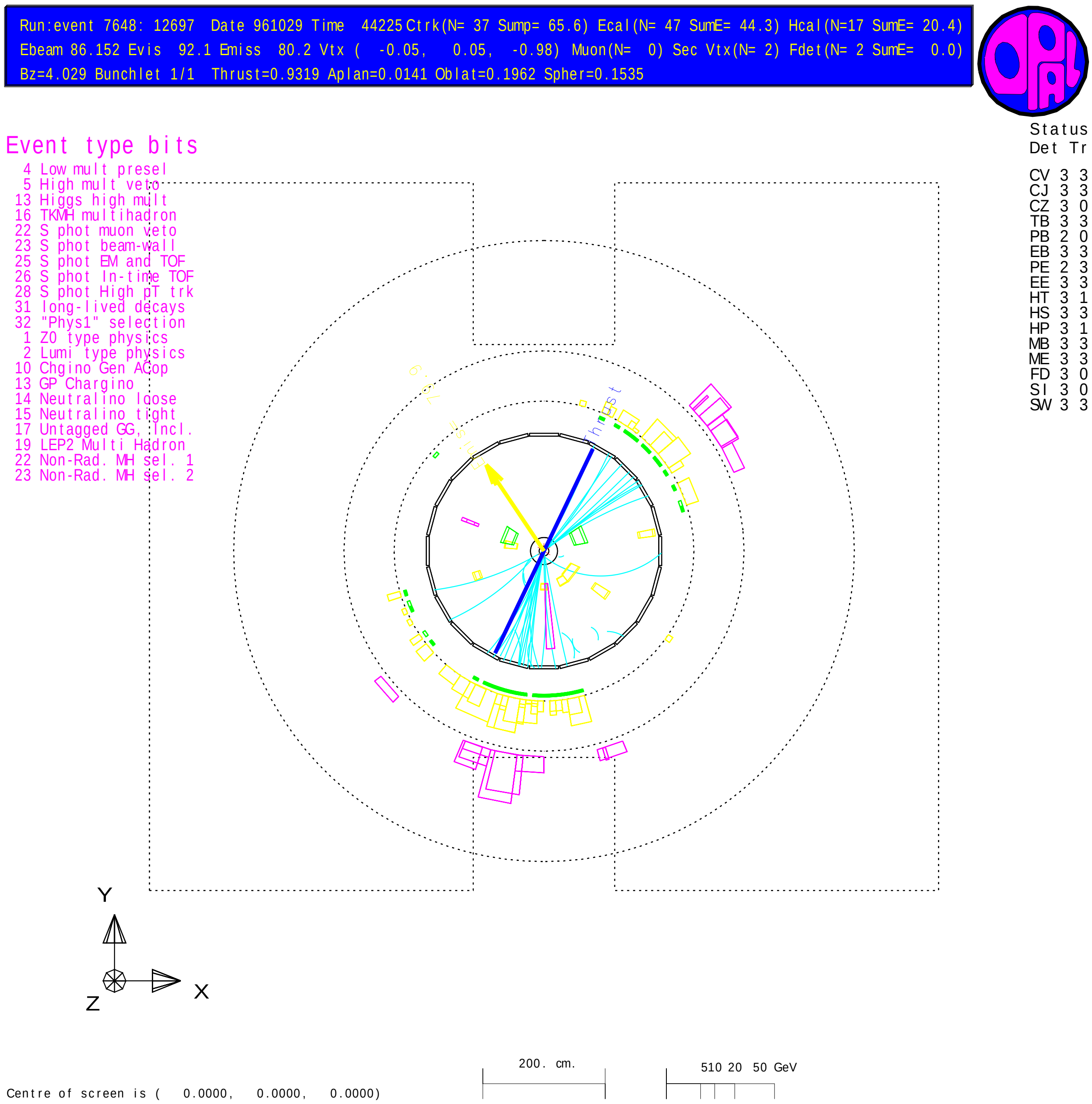

Figure 18: Third selected event: run 7648, event 12697, $\sqrt{s} = 172$ GeV, $\not{p}_t = 32.2$ GeV/c, $\phi_{\text{acop}} = 33.4°$, $E_{miss} = 35.6$ GeV, $M_{\text{q}\overline{\text{q}}'} = 82.1$ GeV/c^2.

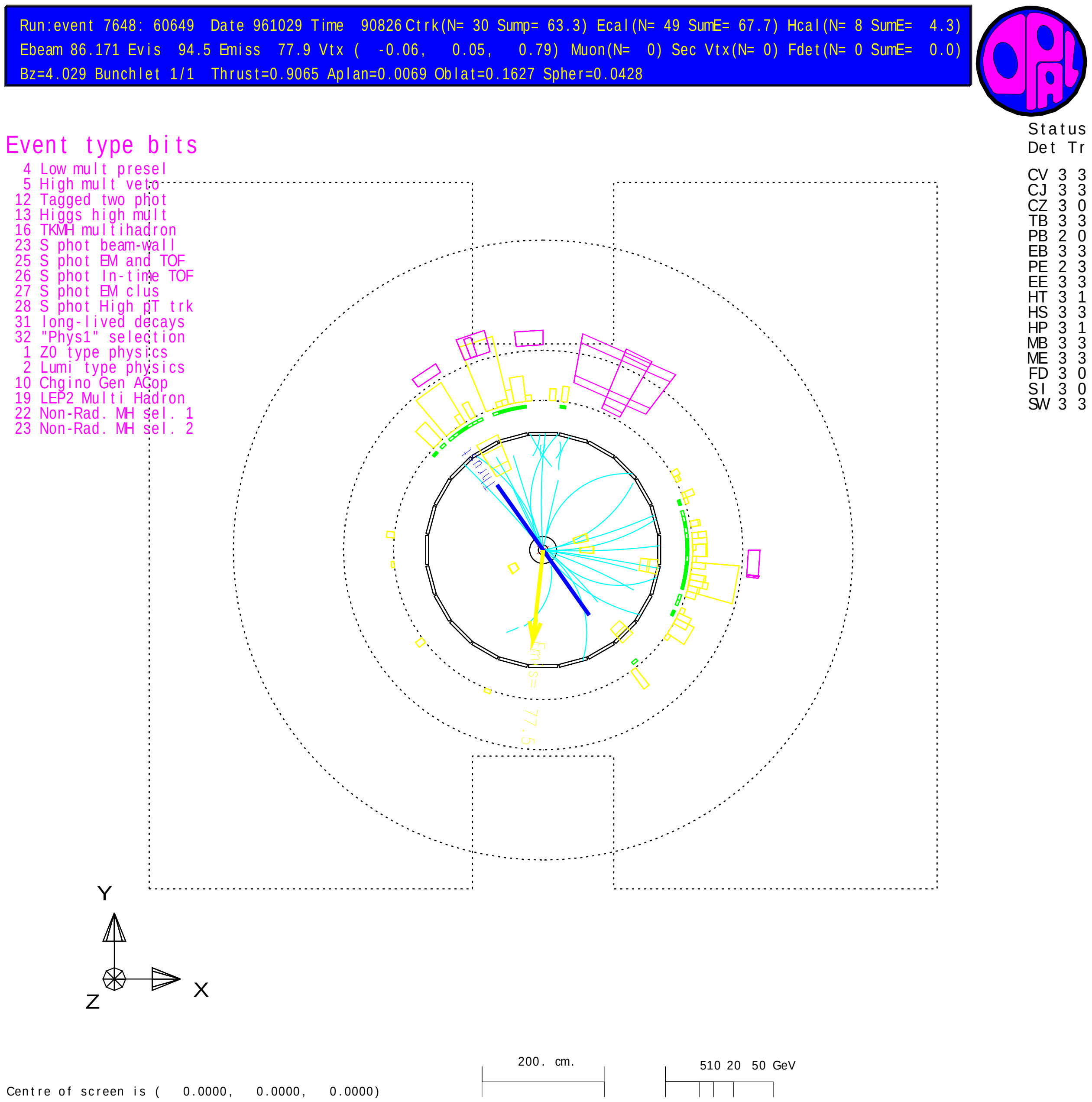

Figure 19: Fourth selected event: run 7648, event 60649, $\sqrt{s} = 172$ GeV, $\not p_t = 35.4$ GeV/c, $\phi_{\rm acop} = 59.0^\circ$, $E_{miss} = 43.2$ GeV, $M_{\rm q\overline{q}'} = 84.7$ GeV/c^2.

Appendix E Efficiency selection

The selection efficiency is given in table 9 for $\sqrt{s} = 161$ and 172 GeV as a function of the anomalous couplings κ_γ and λ_γ, for the two treatments of the initial state radiation (SF and PS). In the cross section fit a linear interpolation between different values of κ_γ and λ_γ is independently performed and then a correction is applied depending on the minimal distance from the $\lambda_\gamma = 0$ or the $\kappa_\gamma = 1$ axes. In the interesting region this correction is at most 5%. The generation of additional Monte Carlo samples would enable a better determination of this correction factor and its relative uncertainty.

κ_γ	λ_γ	$\sqrt{s} = 161$ GeV		$\sqrt{s} = 172$ GeV	
		ϵ_{SF} (%)	ϵ_{PS} (%)	ϵ_{SF} (fb)	ϵ_{PS} (%)
1.00	0.00	42.1±1.3	40.5±1.3	34.0±1.2	29.7±1.2
1.50	0.00	43.6±1.2	42.2±1.3	32.1±1.2	32.5±1.2
2.00	0.00	43.9±1.2	42.4±1.2	35.9±1.2	33.5±1.2
3.00	0.00	44.4±1.2	44.0±1.2	35.3±1.2	36.2±1.2
5.00	0.00	44.7±1.2	44.5±1.2	36.2±1.2	35.6±1.2
0.50	0.00	42.6±1.4	40.0±1.4	31.8±1.3	29.5±1.2
0.00	0.00	43.9±1.5	43.1±1.5	35.1±1.5	36.8±1.5
-1.00	0.00	50.6±1.3	51.3±1.3	41.8±1.3	40.6±1.3
-3.00	0.00	47.4±1.2	48.0±1.2	41.5±1.2	38.4±1.2
1.00	1.00	46.5±1.3	45.0±1.3	39.8±1.2	37.4±1.3
1.00	2.00	50.0±1.2	47.5±1.3	45.7±1.2	41.2±1.2
1.00	4.00	54.6±1.2	51.1±1.2	49.7±1.2	48.1±1.2
1.00	-1.00	46.0±1.3	40.7±1.3	38.7±1.2	36.4±1.3
1.00	-2.00	49.9±1.2	46.9±1.2	42.3±1.2	38.6±1.2
1.00	-4.00	53.5±1.2	51.8±1.2	48.3±1.2	46.3±1.2
3.00	2.00	47.8±1.2	44.3±1.2	37.6±1.2	37.9±1.2
3.00	-2.00	47.6±1.2	48.1±1.2	39.7±1.2	37.6±1.2
-1.00	2.00	57.8±1.2	57.4±1.3	51.4±1.2	50.1±1.2
-1.00	-2.00	48.0±1.2	47.0±1.2	45.9±1.2	42.6±1.3

Table 9: Selection efficiency as function of the anomalous couplings κ_γ and λ_γ.